NeuroResource

Neuron

Neural Circuit-Specialized Astrocytes: Transcriptomic, Proteomic, Morphological, and Functional Evidence

Highlights

- Multiple approaches were used to assess astrocyte diversity in two neural circuits
- Physiological and anatomical studies showed evidence for astrocyte functional diversity
- RNA-seq, proteomic, and cell marker analyses confirmed diversity
- Evidence is provided for brain neural-circuit-specialized astrocytes

Authors

Hua Chai, Blanca Diaz-Castro, Eiji Shigetomi, ..., Julian P. Whitelegge, Giovanni Coppola, Baljit S. Khakh

Correspondence

bkhakh@mednet.ucla.edu

In Brief

The Khakh lab used state-of-the-art optical, anatomical, electrophysiological, transcriptomic, and proteomic approaches to explore astrocyte similarities and differences in two neural circuits. Candid evaluation of the data across ten approaches provided not only strong evidence for astrocyte diversity but also an experimental workflow to explore astrocyte diversity across the brain.

Chai et al., 2017, Neuron *95*, 1–19
August 2, 2017
http://dx.doi.org/10.1016/j.neuron.2017.06.029

CellPress

Please cite this article in press as: Chai et al., Neural Circuit-Specialized Astrocytes: Transcriptomic, Proteomic, Morphological, and Functional Evidence, Neuron (2017), http://dx.doi.org/10.1016/j.neuron.2017.06.029

Neuron
NeuroResource

Neural Circuit-Specialized Astrocytes: Transcriptomic, Proteomic, Morphological, and Functional Evidence

Hua Chai,[1,12] Blanca Diaz-Castro,[1,12] Eiji Shigetomi,[1,3] Emma Monte,[4] J. Christopher Octeau,[1] Xinzhu Yu,[1] Whitaker Cohn,[5,6] Pradeep S. Rajendran,[7] Thomas M. Vondriska,[1,4,8] Julian P. Whitelegge,[5,6] Giovanni Coppola,[9,10,11] and Baljit S. Khakh[1,2,13,*]

[1]Department of Physiology
[2]Department of Neurobiology
David Geffen School of Medicine, University of California, Los Angeles, Los Angeles, CA 90095-1751, USA
[3]Department of Neuropharmacology, Interdisciplinary Graduate School of Medicine, University of Yamanashi, Yamanashi 409-3898, Japan
[4]Department of Anesthesiology
[5]Pasarow Mass Spectrometry Laboratory, Semel Institute for Neuroscience and Human Behavior
[6]Brain Research Institute
[7]UCLA Cardiac Arrhythmia Center, Neurocardiology Research Center for Excellence
[8]Department of Medicine
[9]Department of Neurology
[10]Department of Psychiatry and Biobehavioral Sciences
[11]Center for Neurobehavioral Genetics, Semel Institute for Neuroscience and Human Behavior
David Geffen School of Medicine, University of California, Los Angeles, Los Angeles, CA 90095-1751, USA
[12]These authors contributed equally
[13]Lead Contact
*Correspondence: bkhakh@mednet.ucla.edu
http://dx.doi.org/10.1016/j.neuron.2017.06.029

SUMMARY

Astrocytes are ubiquitous in the brain and are widely held to be largely identical. However, this view has not been fully tested, and the possibility that astrocytes are neural circuit specialized remains largely unexplored. Here, we used multiple integrated approaches, including RNA sequencing (RNA-seq), mass spectrometry, electrophysiology, immunohistochemistry, serial block-face-scanning electron microscopy, morphological reconstructions, pharmacogenetics, and diffusible dye, calcium, and glutamate imaging, to directly compare adult striatal and hippocampal astrocytes under identical conditions. We found significant differences in electrophysiological properties, Ca^{2+} signaling, morphology, and astrocyte-synapse proximity between striatal and hippocampal astrocytes. Unbiased evaluation of actively translated RNA and proteomic data confirmed significant astrocyte diversity between hippocampal and striatal circuits. We thus report core astrocyte properties, reveal evidence for specialized astrocytes within neural circuits, and provide new, integrated database resources and approaches to explore astrocyte diversity and function throughout the adult brain.

INTRODUCTION

Astrocytes exist throughout the brain and tile the nervous system. Astrocytes are morphologically complex cells with thousands of processes that create characteristically "bushy" territories. The finest processes contact synapses, blood vessels, and other glia, where they mediate multiple supportive, active, and homeostatic roles (Khakh and Sofroniew, 2015). Astrocytes are also involved in disease, as evidenced by analyses of postmortem human brains and from extensive cell culture and mouse model studies (Chung et al., 2015a).

Despite important progress, astrocytes remain an understudied cell population, and much remains to be explored. Unlike neurons, which are extremely diverse, astrocytes are viewed as a largely homogeneous population of cells. This raises an important question: how can astrocytes be largely interchangeable and yet mediate their many separable responses? One hypothesis that has been recently advanced to explain this quandary is the possibility that astrocytes are not a homogeneous population of glue-like cells in different neural circuits (Ben Haim and Rowitch, 2017; Khakh and Sofroniew, 2015; Zhang and Barres, 2010). Despite being frequently invoked, with the exception of spinal cord development (Molofsky et al., 2014), this hypothesis is incompletely tested, although there is emerging evidence to support it in the context of aging and disease (John Lin et al., 2017; Soreq et al., 2017). Moreover, the finding that reactive astrocytes are different from healthy astrocytes (Liddelow et al., 2017; Zamanian et al., 2012) does not directly prove astrocyte diversity; rather, these

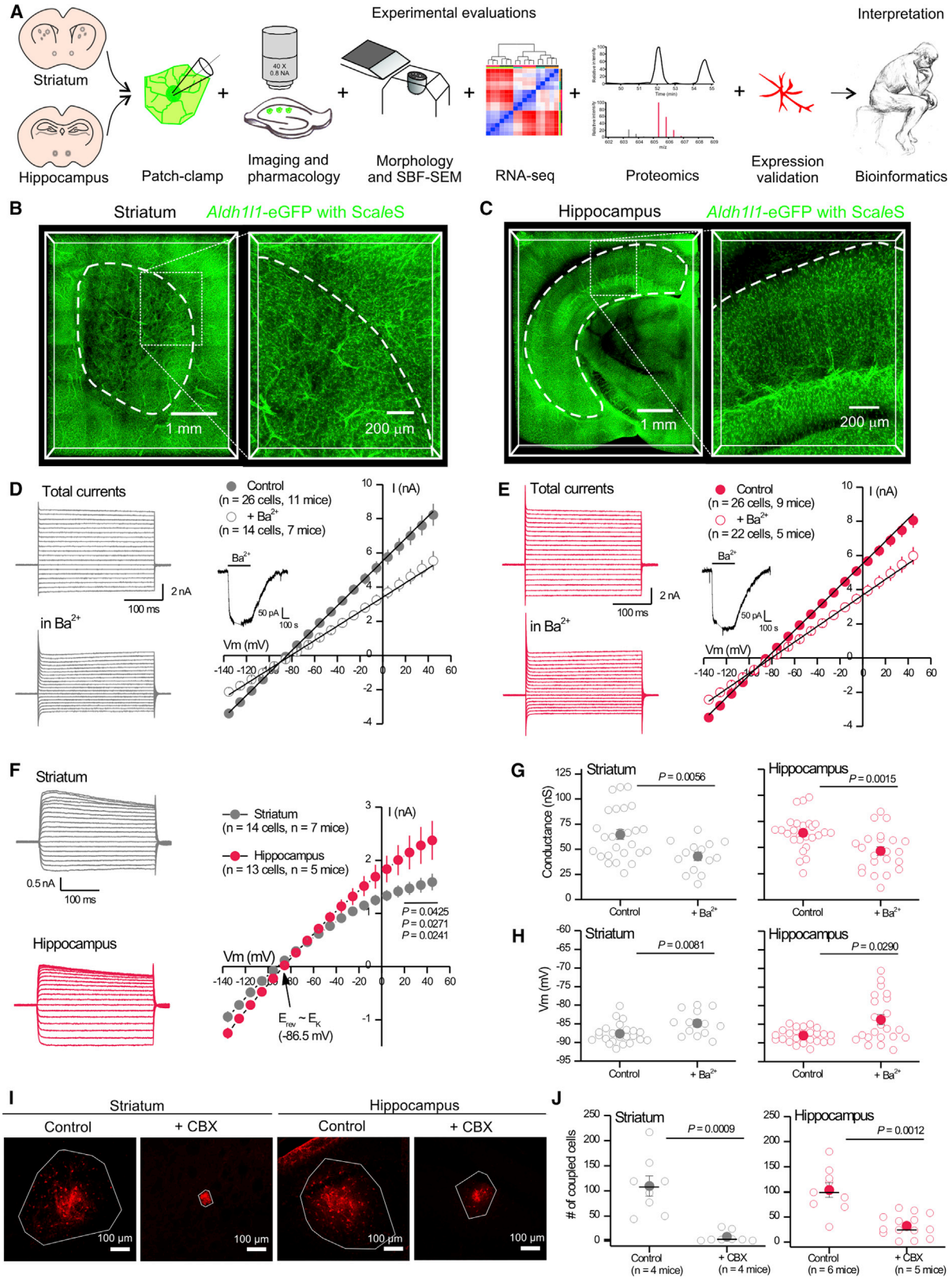

(legend on next page)

studies show that astrocytes change in important ways when they are challenged.

We sought to determine if astrocytes within two distinct, mature brain neural circuits were largely similar or distinct when assessed using a range of integrated approaches that would permit candid assessment of diversity at multiple biological levels. In designing our study, we benefitted from the demonstration of interneuron diversity, which emphasizes evaluations using physiology, morphology, as well as gene, protein, and cell marker expression (Kepecs and Fishell, 2014). We also chose two exemplar neural circuits to test the hypothesis: the striatum and hippocampus. The striatum is the major nucleus of the basal ganglia: it integrates converging excitatory and inhibitory signals from numerous parts of the brain and is involved in action selection, habit formation, and motor function (Graybiel, 2008). The hippocampal CA1 region is the site of the majority of hippocampal output and is necessary, among other things, for establishing long-term explicit memory. The striatum consists mainly of inhibitory GABAergic medium spiny neurons (Graybiel, 2008), whereas the hippocampus comprises mainly excitatory glutamatergic neurons (Spruston and McBain, 2007).

Critical functions have been ascribed to astrocytes in both the hippocampus and striatum (Araque et al., 2014; Khakh and Sofroniew, 2015), but as is true for other brain areas, it is unclear how potentially interchangeable cells serve such diverse roles in hippocampal and striatal neural circuits, which themselves operate by utilizing distinct neuronal populations. Thus, the necessity to address astrocyte diversity at a basic biology level, the relevance to disease and neural circuit function, and the availability of new tools presented an opportunity to determine if astrocytes in the striatum and hippocampus were largely similar or if they displayed neural circuit specificity.

RESULTS

We used multiple evaluations to compare adult striatal and hippocampal astrocytes under identical conditions (Figure 1A). The single-cell evaluations were performed for astrocytes in the dorsolateral (d.l.) striatum and hippocampus CA1 stratum radiatum (s.r.).

Astrocyte Density and Electrophysiological Properties in Striatum and Hippocampus

Astrocyte regional density varies (Khakh and Sofroniew, 2015), and it has been suggested that the striatum contains low astrocyte numbers (Cui et al., 2016). We therefore began by comparing the density of astrocytes in the hippocampus and striatum using Sca*l*eS brain clearing and *Aldh1l1*-EGFP reporter mice, which label most astrocytes (Cahoy et al., 2008; Treweek and Gradinaru, 2016). We found that astrocyte densities were equally high for d.l. striatum and hippocampus CA1 s.r. at 8 ± 2 and 11 ± 1 astrocytes per 100 μm cube, respectively (Figures 1B and 1C; Movie S1; $p > 0.05$, $n = 3$ mice).

We next used patch-clamp electrophysiology to directly compare hippocampal CA1 s.r. and d.l. striatal astrocytes (Figures 1D–1H). We recorded the current-voltage relation, slope conductance, and resting membrane potential (Vm) under control conditions and in the presence of 300 μM Ba^{2+} (Figures 1D–1H) to block Kir4.1 channels. The basic membrane properties of astrocytes in the striatum and hippocampus were similar (Table S1) and Ba^{2+} was effective at reducing the membrane conductance and in depolarizing Vm (Figures 1G and 1H). However, the Ba^{2+}-sensitive currents were larger in the hippocampus than in the striatum at Vm values with greatest driving force (Figure 1F). The Ba^{2+}-sensitive currents reversed (−86.5 mV) close to the K^+ equilibrium potential.

Astrocytes form extensive networks of coupled cells. We dialyzed single astrocytes via the patch pipette with biocytin, a gap-junction-permeable molecule, and post hoc assessed the extent of gap-junctional coupling. Under identical conditions, we found that the network of coupled astrocytes at ~100 cells was not significantly different between the hippocampus and striatum, and in both brain areas, the gap junction blocker carbenoxolone (CBX; 100 μM) significantly reduced coupling (Figures 1I and 1J). However, in the presence of CBX, the extent of remaining gap-junctional coupling was significantly higher in the hippocampus (32 ± 6 cells) than the striatum (8 ± 4 cells; Figure 1J; $p = 0.0239$). Thus, there were significant physiological differences between astrocytes located in the d.l. striatum and hippocampus CA1 s.r.

Astrocyte Ca^{2+} Signaling in d.l. Striatum and Hippocampus CA1 s.r.

Intracellular Ca^{2+} signaling is an important aspect of astrocyte biology (Shigetomi et al., 2016). In accord, a rich panoply of spontaneous Ca^{2+} signals can be visualized with genetically encoded calcium indicators (GECIs) such as GCaMP6f. GECIs and other reporters can be selectively delivered to astrocytes (Figure S1) using adeno-associated viruses (AAVs) without detectable astrogliosis (Haustein et al., 2014; Jiang et al., 2016; Rungta et al.,

Figure 1. Astrocyte Physiological Similarities and Differences in Striatum and Hippocampus

(A) Approaches used to evaluate striatal and hippocampal astrocytes (SBF-SEM, serial block-face-scanning electron microscopy).

(B and C) Coronal sections of *Aldh1l1*-EGFP brains cleared using Sca*l*eS and imaged using confocal microscopy for striatum (B) and hippocampus (C).

(D and E) Whole-cell voltage clamp was performed on d.l. striatal (D) and CA1 s.r. (E) astrocytes before and in the presence of 300 μM Ba^{2+}. Left: example waveforms for total and Ba^{2+}-insensitive currents. Right: average current-voltage relations. Inset: application of Ba^{2+} caused a reversible decrease in membrane current at −70 mV; the gap is when recording was paused for current-voltages (IVs).

(F) Ba^{2+}-sensitive currents.

(G and H) Membrane conductance (G) and membrane potential (H) of d.l. striatal and CA1 s.r. astrocytes for control and in 300 μM Ba^{2+}.

(I) Representative images of biocytin (30 min; red) filled astrocyte syncytium in the d.l. striatum and hippocampus CA1 s.r. with and without 100 μM CBX to block gap junctions. The white polygon delineates dye spread.

(J) The number of coupled EGFP-positive astrocytes in control and in the presence of 100 μM CBX. Open circles represent raw data, closed circles indicate mean ± SEM, and a horizontal line represents the median. In some cases, the error bars representing SEM are smaller than the symbol used for the mean. Average data are shown as mean ± SEM.

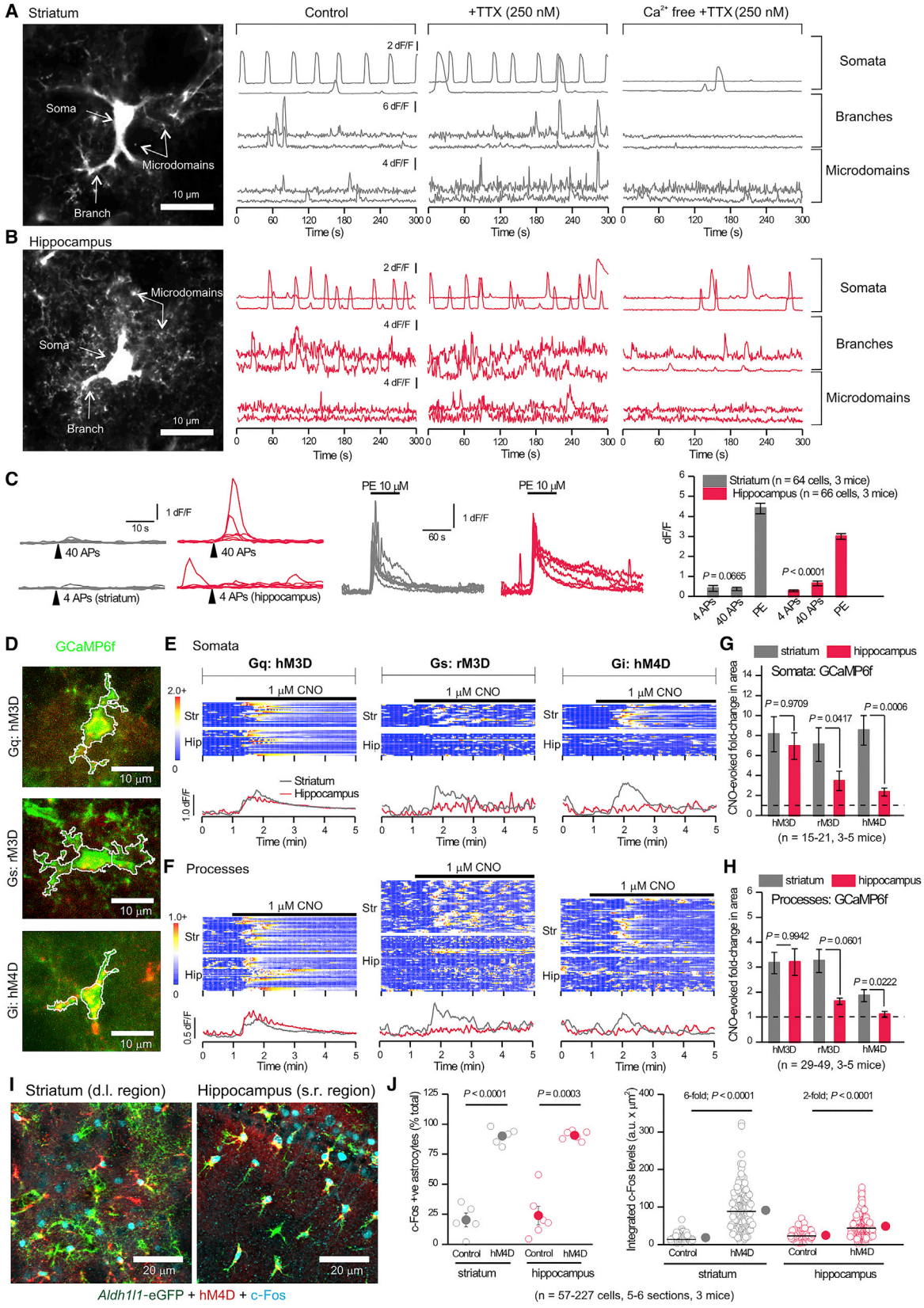

(legend on next page)

2016; Shigetomi et al., 2013). Using such methods, we assessed Ca^{2+} signals in astrocyte somata, major branches, and microdomains in processes (Figures 2A and 2B; Table S2; Movie S2).

To determine if astrocyte Ca^{2+} signals were caused by neuronal activity, we applied 250 nM tetrodotoxin (TTX) to block action potentials (APs). TTX did not decrease the frequency of astrocyte Ca^{2+} signals in somata, branches, or microdomains in either brain region (Figures 2A, 2B, and S2B), nor did it decrease their amplitude or duration (Table S2). Hence, in adult mouse astrocytes, spontaneous Ca^{2+} signals are not caused by ongoing AP-dependent neuron-astrocyte interactions. Since astrocyte Ca^{2+} signals vary in their dependence on Ca^{2+} entry and release from stores, we applied Ca^{2+}-free extracellular buffers. The example traces and pooled data show dramatic reductions in the frequency of spontaneous Ca^{2+} signals in all compartments for both d.l. striatal and hippocampal CA1 s.r. astrocytes (Figures 2A, 2B, and S2B). The effect of Ca^{2+}-free buffers was equivalent between the striatum and hippocampus, indicating similar dependence on Ca^{2+} entry for spontaneous signals (Figure S2B).

Spontaneous Ca^{2+} signal frequency was higher in the hippocampus than striatum under control conditions ($p = 0.0469$; Figure S2A; Table S2), in TTX ($p = 0.0165$) and in Ca^{2+}-free conditions ($p = 0.0228$; Figure S2B). We examined the somatic events more closely and classified them as global events that encompassed the entire soma and some major branches or as non-global events that included only a subregion (Figure S2C). In control conditions, a significantly greater proportion of somatic events in hippocampal astrocytes were global events (Figure S2C; $p = 0.0052$). Although the frequency of somatic events decreased significantly with removal of extracellular Ca^{2+} (Figures 2A, 2B, and S2B), global events were relatively spared in Ca^{2+}-free conditions, indicating an intracellular origin (Figure S2C). The inter-regional difference remained significant in Ca^{2+}-free buffers (Figure S2C; $p = 0.032$). We also assessed Ca^{2+} homeostasis in striatal and hippocampal astrocytes using store-depletion protocols. Astrocytes from the striatum relied more heavily on extracellular entry for basal Ca^{2+} levels than astrocytes from the hippocampus (Figure S2D; $p = 0.0199$). Other aspects were similar ($p > 0.05$; Figure S2D). Hence, both hippocampal and striatal astrocytes display spontaneous Ca^{2+} signals, but with some marked differences.

We assessed AP-dependent evoked astrocyte Ca^{2+} signals in d.l. striatal and hippocampal CA1 s.r. astrocytes following electrical field stimulation (EFS) of cortical and Schaffer-collateral inputs (Figure 2C). In accord with recent studies (Shigetomi et al., 2016), we found that striatal and hippocampal astrocytes responded equally weakly to EFS of glutamatergic input during brief trains of EFS (four APs at 10 Hz, $p = 0.45123$; Figure 2C). Hippocampal astrocytes responded more reliably to longer trains (40 APs at 10 Hz), but striatal astrocytes did not (Figure 2C). Astrocytes in both areas responded strongly to bath application of the α1 adrenoceptor agonist phenylephrine (10 μM; Figure 2C). Later, we report differences in EFS-evoked glutamate release onto astrocytes.

Astrocyte GPCR-Mediated Ca^{2+} Signaling in d.l. Striatum and Hippocampus CA1 s.r.

Astrocytes express Gq, Gi/o, and Gs G-protein-coupled receptors (GPCRs) that may mediate Ca^{2+} signals. We explored if d.l. striatal and hippocampal CA1 s.r. astrocytes differed in the ability of GPCR pathways to evoke Ca^{2+} signals (in 250 nM TTX). We began by using designer receptors exclusively activated by designer drugs (DREADDs) expressed in astrocytes (Figure 2D) to selectively stimulate GPCR Gq, Gs, and Gi pathways with hM3D, rM3D, and hM4D DREADDs, respectively (Roth, 2016). Each of these receptors was activated by clozapine-N-oxide (CNO). In astrocytes expressing hM3D, 1 μM CNO evoked robust and equivalent increases in intracellular Ca^{2+} in hippocampal and striatal astrocyte somata and processes (Figures 2E and 2F). Activation of rM3D and hM4D with CNO also increased Ca^{2+} in striatal astrocytes, but the effects of activating Gs or Gi DREADDs were smaller in hippocampal astrocytes (Figures 2E and 2F). The similarities between activating hM3D for striatal and hippocampal astrocytes, and the differences between activating rM3D and hM4D, were evident from the kymographs and average traces (Figures 2E and 2F). To quantify these data, we plotted the CNO-evoked fold change in GCaMP6f fluorescence and compared this between striatal and hippocampal astrocytes, which confirmed the differences statistically (Figures 2G and 2H). Since Gi-coupled hM4D-evoked Ca^{2+} responses exhibited the greatest differences, we examined the effects on c-Fos expression. Activating striatal and hippocampal astrocytes expressing hM4D in vivo with CNO (1 mg/kg) increased c-Fos-expressing astrocytes in both the striatum and hippocampus (Figures 2I and 2J) but caused a greater increase in c-Fos levels in striatal astrocytes (Figure 2J). Thus, differences between hippocampal and striatal

Figure 2. Properties of Ca^{2+} Signals in Striatal and Hippocampal Astrocytes

(A and B) Left: projections of GCaMP6f expressing d.l. striatal (A) and hippocampal CA1 s.r. (B) astrocytes; arrows indicate compartments with Ca^{2+} signals. Right: representative traces of GCaMP6f dF/F for control, 0.25 μM TTX, and Ca^{2+}-free extracellular buffers with TTX (Figure S2).

(C) EFS of cortical input to the d.l. striatum and EFS of Schaffer-collaterals in the hippocampus CA1 s.r. evoked modest Ca^{2+} signals. Phenylephrine (PE) evoked large Ca^{2+} elevations.

(D) Example images of astrocytes co-expressing GCaMP6f (green) and each of the three mCherry-tagged DREADDs (red).

(E) Top: kymographs of astrocyte somatic Ca^{2+} signals (GCaMP6f dF/F) upon activation of DREADDs with 1 μM CNO. Each row represents a single cell. Bottom: average traces from d.l. striatal (gray) and hippocampal CA1 s.r. (red) astrocytes (n = 15–21 cells from three to five mice).

(F) As in (E), but for astrocyte process Ca^{2+} signals (n = 29–49, three to five mice).

(G and H) Average CNO-evoked fold-change in area under the curve for astrocyte somata (G) and processes (H).

(I) Representative images show hM4D-expressing (red) astrocytes (green) with increased levels of c-Fos (cyan) 1 hr after 1 mg/kg CNO.

(J) The percentage of c-Fos positive astrocytes and the integrated c-Fos intensity. Raw data are shown with open circles; closed circles indicate the mean ± SEM. The median is shown with a line. Data were collected from five or six sections from three mice.

Average data are shown as mean ± SEM.

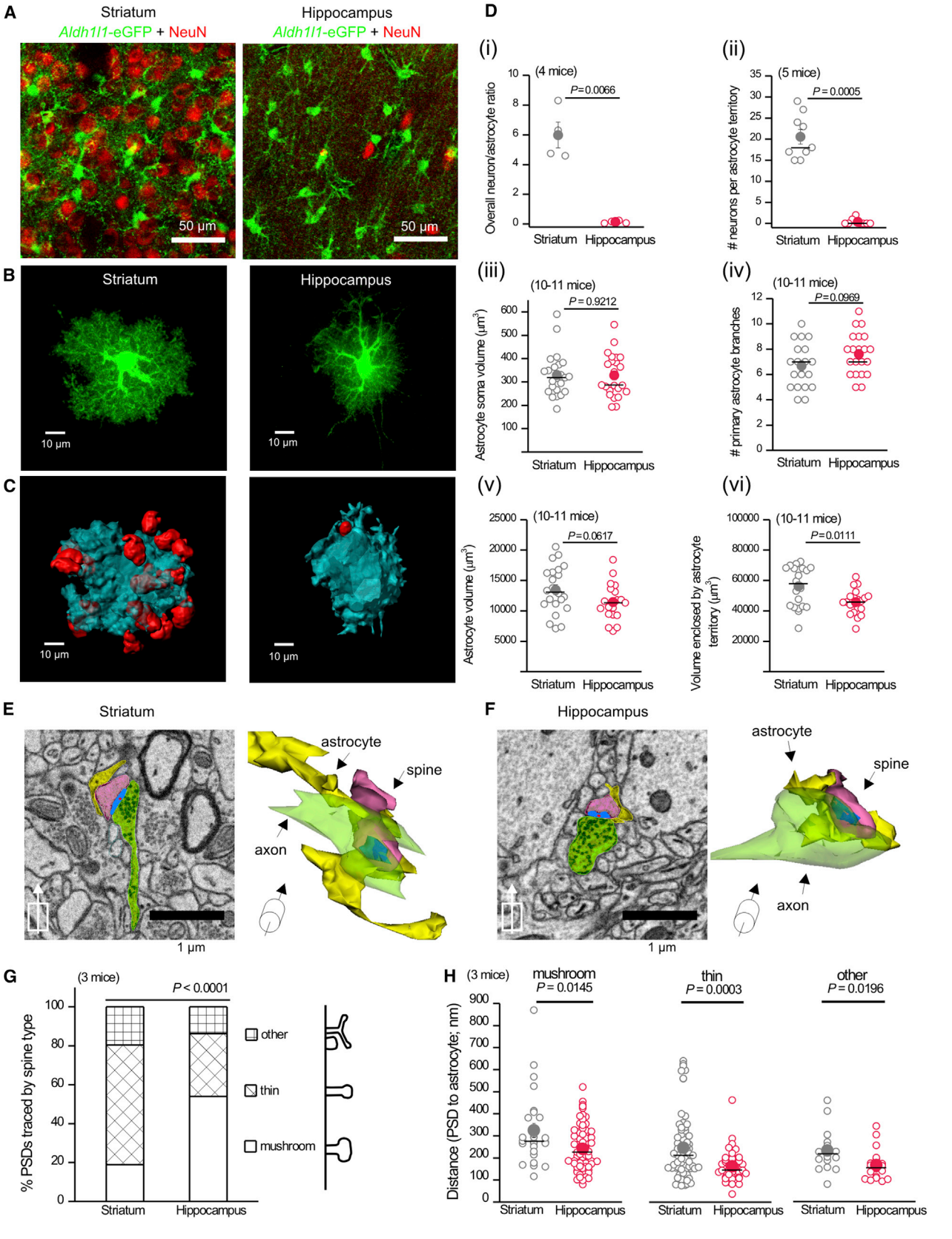

(legend on next page)

astrocytes in terms of Gi-coupled GPCR signaling may be reflected as differences in gene expression regulation.

Next, we tested whether Ca^{2+} signals evoked by activation of endogenous GPCRs were different between d.l. striatal and hippocampal CA1 s.r. astrocytes. Consistent with past work, α1 adrenoceptor agonist phenylephrine (10 μM) evoked similarly robust increases in striatal and hippocampal astrocyte Ca^{2+} (Figure S3). However, the response to 100 μM DHPG, the agonist for mGluR1/5 receptors, was weak in both regions (Figure S3C), consistent with the finding that this receptor is downregulated in adult astrocytes (Haustein et al., 2014; Srinivasan et al., 2016; Sun et al., 2013). We also tested Gi/o-coupled mGluR2/3 agonist LY354740 and measured robust Ca^{2+} signals in striatal somata and processes but no significant signals for hippocampal astrocytes (Figure S3), which extends the hM4D DREADD data (Figure 2E–2H). However, activation of Gi/o-coupled $GABA_B$ GPCRs (50 μM R-baclofen) evoked similar responses in striatal and hippocampal astrocytes (Figure S3C). The striatum receives dense dopaminergic input; however, we observed weak responses to activation of Gs-coupled $D_{1/5}$ receptors and Gi/o-coupled D_2 and D_3 receptors (by 10 μM A77636, 10 μM sumanirole, and 50 μM PD128907) in striatal astrocytes (Figure S3C). Hippocampal astrocytes showed a similarly weak response. We note that agonists at endogenous GPCRs are not as specific as the use of DREADDS, because they may have actions at other cells within slices. Hence, we draw the robust conclusion based on results from the use of DREADDs as guided by results from endogenous GPCRs that activation of Gq was equally effective in striatal and hippocampal astrocytes but that activation of Gi/o was significantly more effective in striatal astrocytes.

d.l. Striatal and Hippocampal CA1 s.r. Astrocyte Morphology Assessed with Light Microscopy

By using *Aldh1l1*-EGFP reporter mice and NeuN staining (Figure 3A), we measured the ratio of neurons to astrocytes in the d.l. striatum and hippocampus CA1 s.r. and found significant differences (Figure 3Di). Thus, the level of neuronal investment is distinct, despite the fact that both regions have similar astrocyte density (Figures 1B and 1C). We next used intracellular iontophoresis of Lucifer yellow (LY) in lightly fixed brain tissue (Bushong et al., 2002) to assess astrocyte morphology (Figure 3B). LY filling of astrocytes revealed their bushy shapes (Movie S3). Using 3D reconstructions, we determined the volumes enclosed by single astrocytes (Figure 3C). NeuN co-staining of LY-filled astrocytes showed that ~20 neuronal cell bodies intersected with a single d.l. striatal astrocyte territory, whereas at most one neuronal cell body intersected with hippocampal CA1 s.r. astrocytes (Figures 3C and Dii). We also found that striatal and hippocampal astrocytes displayed equivalent somatic volumes, the same number of primary branches, and the same cell volumes (Figure 3Diii–v). However, the territory volume of striatal astrocytes was significantly larger than that of hippocampal astrocytes (Figure 3Dvi). The density of excitatory synapses in the rat striatum and hippocampus is ~0.9 and ~2.0 per μm^3 (Harris et al., 1992; Ingham et al., 1998), implying that single striatal and hippocampal astrocyte territories encompass ~50,700 and ~95,200 excitatory synapses, respectively. Hence, striatal astrocyte territories are larger than hippocampal ones and impinge upon significantly greater numbers of neuronal somata, but hippocampal astrocyte territories contain more excitatory synapses.

d.l. Striatal and Hippocampal CA1 s.r. Astrocyte-Synapse Proximity Assessed with SBF-SEM

We used serial block-face scanning electron microscopy (SBF-SEM) to examine the proximity and interaction of astrocyte processes, presynaptic terminals, and postsynaptic spines in the d.l. striatum and hippocampus CA1 s.r. (Figures 3E and 3F; Movie S4; n = 3 mice). In the striatum, the majority of excitatory spines were thin (Figure 3G), consistent with published data (Bello-Medina et al., 2016). The majority in the hippocampus were mushroom spines (Figure 3G), highlighting differences in the environments of striatal and hippocampal astrocytes. To evaluate whether astrocyte interactions with synapses differed between the two regions, we measured the vector between astrocyte processes and the center of the postsynaptic density (PSD). We found that striatal astrocyte processes were further away from PSD centers for all types of spines (Figure 3H). In addition, fewer synaptic interfaces in the striatum displayed astrocytic contacts (77% in striatum and 86% in hippocampus, Fisher's exact test p = 0.04486). Within either region, astrocyte processes were located more distally to mushroom spine PSDs when compared to other spines (Figure 3H). This is expected as mushroom spines have larger volumes and bigger PSDs (Arellano et al., 2007). Astrocyte morphology at the cellular and ultrastructural levels suggests that hippocampal astrocytes

Figure 3. Comparison of d.l. Striatal and Hippocampal CA1 s.r. Astrocyte Morphology and Proximity to Synapses

(A) Representative z-projection of *Aldh1l1*-EGFP d.l. striatum and hippocampus CA1 s.r. sections immunostained for GFP (green) and NeuN (red).

(B) Confocal volumes of Lucifer yellow filled astrocytes in wild-type mice.

(C) Three-dimensional reconstructions of volumes enclosed by astrocyte territories (blue) and NeuN (red).

(D) The ratio of green astrocytes and red neurons quantified from confocal images as shown in (A) from four mice (i). Number of neurons in a single astrocyte territory as determined by reconstructions in (C) (ii). (iii–vi) Astrocyte somata volume (iii), the number of primary branches (iv), astrocyte cell volume (v), and astrocyte territory volume (vi) were compared for striatal and hippocampal astrocytes (n = 19–22 from 10–11 mice).

(E) Example of scanning electron microscopy (EM) image from the d.l. striatum with corresponding 3D rendering. The synaptic structures and closest astrocyte processes are colored as: yellow astrocytes, blue postsynaptic densities (PSDs), green axons, and pink spines. The center of the PSD is denoted with a red dot.

(F) As in (E), but for hippocampus CA1 s.r.

(G) The types of excitatory spines were significantly different between striatum and hippocampus (Fisher's exact test, n = 138–139 PSDs from three mice).

(H) The distances between centers of the PSD and nearest astrocyte process are shown according to the spine type of the PSD (mushroom, n = 27–75; thin, n = 45–95; other, n = 16–19 synapses). Open circles are raw data (from three mice), with closed circles indicating mean ± SEM and a horizontal line the median. In some cases, the error bars representing SEM are smaller than the symbol used to show the mean.

Average data are shown as mean ± SEM.

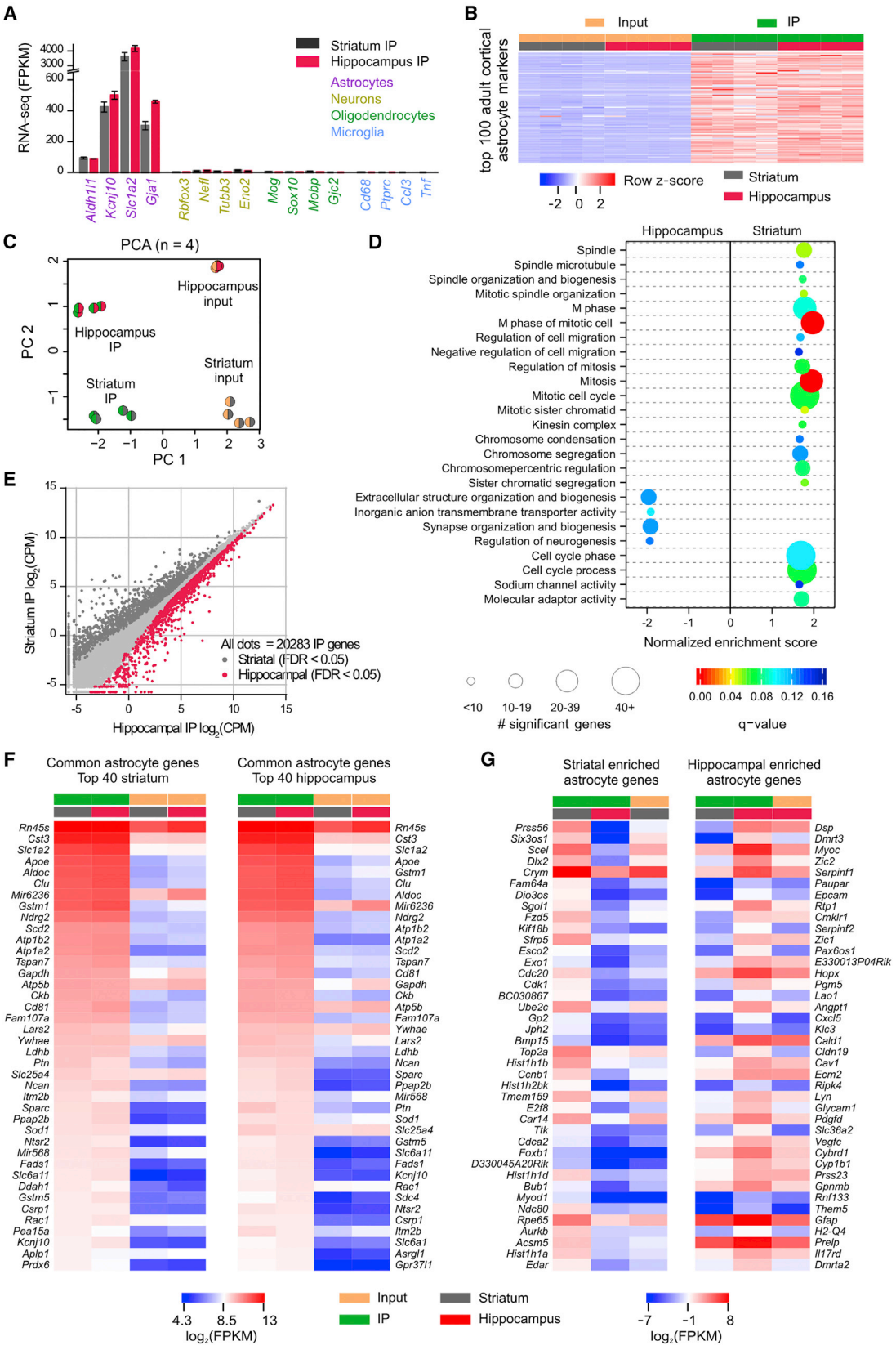

(legend on next page)

occupy smaller territories but display significantly greater and tighter physical interactions with excitatory synapses than those in the striatum.

Striatal and Hippocampal Astrocyte Transcriptomes

In addition to evaluations of known astrocyte properties (Figures 1, 2, and 3), we sought unbiased, global understanding of astrocytes in the striatum and hippocampus. To this end, we generated RNA sequencing (RNA-seq) data of adult (postnatal day 63 [P63]) astrocytes from striata and hippocampi using *Aldh1l1*-CreERT2 x RiboTag mice (Sanz et al., 2009). In these mice, the hemagglutinin (HA)-tagged ribosomal subunit Rpl22HA was expressed in astrocytes (Srinivasan et al., 2016). Rpl22HA co-localized with S100β, but not with NeuN, throughout the striatum and hippocampus (Figure S4A–S4F). Rpl22HA expression was sufficient to perform immunoprecipitations (IPs) of Rpl22HA and associated actively translated mRNAs from striata and hippocampi of single mice for RNA-seq (Figure S4G, four mice; Data S1). The IP samples were replete with astrocyte markers (Cahoy et al., 2008) but depleted of markers for neurons, oligodendrocytes, and microglia (Figure 4A). Furthermore, the top 100 adult cortical astrocyte genes (Srinivasan et al., 2016) were enriched in striatal and hippocampal IP samples (Figure 4B).

We used principal component analysis (PCA) to cluster our samples based on the 2,000 most variable genes across all samples. Clustering based on the first two principal components revealed that striatal and hippocampal astrocytes represented distinct cell populations (Figure 4C). We also compared the adult striatal and hippocampal RNA-seq data to adult cortical astrocytes (Srinivasan et al., 2016) and found that cortical and hippocampal astrocytes were the most similar (Figure S5). To understand whether functional groups of genes were different between striatal and hippocampal astrocytes, we ran a gene set enrichment analysis (GSEA; false discovery rate [FDR] or q value < 0.15) on all genes sequenced in striatal and/or hippocampal IP samples as ranked by log ratio (LimmaVoom; no FDR threshold). GSEA revealed 21 gene sets enriched in striatal astrocytes and four gene sets enriched in hippocampal astrocytes (Figure 4D), illustrating that these two populations have functionally relevant molecular differences. Most of the 21 striatal gene sets were related to the cell cycle, cell migration, or chromosome structure. Two of the four gene sets enriched in hippocampal astrocytes (synapse organization and biogenesis, extracellular structure organization and biogenesis) are reminiscent of observations from SBF-SEM that hippocampal astrocyte processes are more closely associated with excitatory synapses (Figure 3H).

A differential expression analysis revealed 2,818 differentially expressed transcripts: 1,180 striatal and 1,638 hippocampal (Figure 4E; Data S1). This represents more than 10% of the genes detected in both IP samples. The set of genes highly expressed in IP, but not differentially expressed between striatum and hippocampus, is also interesting (Figure 4F), as these genes may be involved in core astrocyte functions in the striatum and hippocampus. Indeed, genes known to have functional importance in astrocytes, such as *Slc1a2*, *Sparc*, *Kcnj10*, and *Slc6a11*, were found in the striatal and hippocampal lists of 40 most highly expressed common genes (Figure 4F). Figure 4G reports in order the top 40 most differentially expressed genes between striatal and hippocampal astrocytes. Within these top 40, the most highly expressed striatal astrocyte gene is *Crym*, and the most highly expressed hippocampal astrocyte gene is *Gfap*. The RNA-seq data demonstrate that striatal and hippocampal astrocytes are molecularly distinct cell populations and provide a valuable resource for future hypothesis-driven experiments. The data are available at the Gene Expression Omnibus (GEO: GSE94010) and at http://astrocyternaseq.org.

We mined RNA-seq data for candidate K^+ channel genes (Data S1) that may underlie functional differences (Figures 1D–1H). We found significant expression for nine K^+ channels and two auxiliary subunits in hippocampus and striatum (Figure 5A; fragments per kilobase per million [FPKM] >10). Six were differentially expressed (Figure 5A). Similarly, of the known transmembrane Ca^{2+} flux pathways (Data S1), we found significant gene expression for 23 molecules (FPKM >10), of which 9 were differentially expressed (Figure 5B). These included Ca^{2+}-permeable channels and pumps on the plasma membrane and within intracellular organelles (Figure 5B) and are consistent with the imaging data of Figure 2 showing richness in astrocyte Ca^{2+} signaling. Furthermore, of the 249 known Ca^{2+}-binding EF-hand-containing proteins (Data S1), 68 had FPKM >10 in hippocampal or striatal astrocytes and 18 were differentially expressed (Figure 5C). These data illustrate that astrocytes display a surprising richness in K^+ channels, Ca^{2+} flux pathways, and proteins likely to buffer

Figure 4. Comparison of Adult Striatal and Hippocampal Astrocyte Transcriptomes

(A) Gene expression levels (in fragments per kilobase per million; FPKM) of markers for astrocytes, neurons, oligodendrocytes, and microglia in IP samples (n = 4).

(B) Heatmap representing 16 RNA-seq samples from four mice showing relative enrichment (red) or depletion (blue) of the top 100 adult cortical astrocyte markers. Row *Z* scores were calculated using FPKM.

(C) Striatal and hippocampal astrocyte principal component analysis of the 2,000 most variable genes across 16 samples.

(D) Gene set enrichment analysis with all genes sequenced in striatal and hippocampal IP sample (threshold q-value < 0.15) identified 21 gene sets enriched in striatal astrocytes and four gene sets enriched in hippocampal astrocytes. The size of the circle corresponds to the number of significant genes whereas the color indicates the significance of the regional enrichment based on normalized enrichment score (NES).

(E) In total, 20,283 genes were identified (all dots), of which differential expression analysis comparing striatal (dark gray) and hippocampal (red) IP samples identified 1,180 striatal- and 1,638 hippocampal-enriched astrocyte genes (threshold FDR < 0.05; Data S1).

(F) FPKM heatmaps of the top 40 astrocyte genes that were not differentially expressed between regions as ranked by IP FPKM value. Log_2(FPKM) ranged from 4.3 (blue, relatively low expression) to 13 (red, relatively high expression).

(G) FPKM heatmaps of the 40 most differentially expressed astrocyte genes between striatal and hippocampal astrocytes as ranked by differential expression LimmaVoom log ratio (FPKM > 0.1). The most highly expressed striatal astrocyte gene is *Crym*, and the most highly expressed hippocampal astrocyte gene is *Gfap*. Log_2(FPKM) ranged from −7 (blue, relatively low expression) to 8 (red, relatively high expression).

Average data are shown as mean ± SEM.

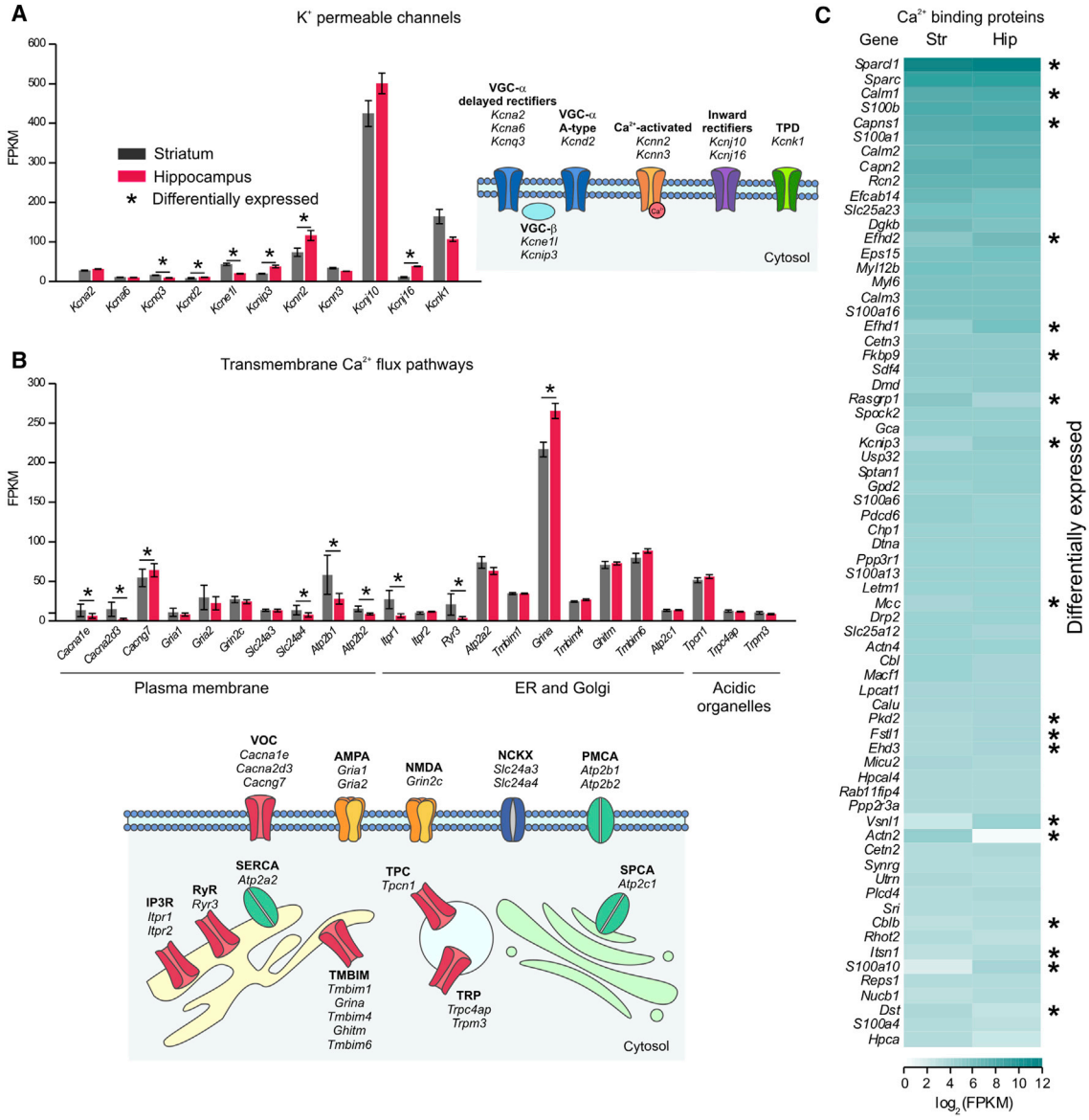

Figure 5. RNA-Seq Analyses of K^+ Channels, Membrane Ca^{2+} Flux Pathways, and Ca^{2+}-Binding Proteins in Striatal and Hippocampal Astrocytes

(A) K^+ channel RNAs that were expressed in astrocytes from striatum or hippocampus with an FPKM > 10.

(B) Ca^+ channel, pump, or exchanger RNAs that were expressed in astrocytes from striatum or hippocampus with an FPKM > 10.

(C) Heatmap representing the average $\log_2$ FPKM values of the Ca^{2+}-binding proteins (four mice), defined by the presence of at least one EF-hand domain, found within striatal and hippocampal astrocytes. Asterisk (*) indicates differential expression between striatal and hippocampal astrocytes using LimmaVoom analysis (FDR < 0.05).

Average data are shown as mean ± SEM.

and respond to Ca^{2+}. The RNA-seq data represent a valuable resource to explore questions related to the electrophysiological and Ca^{2+} signaling properties of astrocytes.

Assessment of Striatal and Hippocampal Astrocyte Proteomes by Mass Spectrometry

Ideally, RNA and protein expression should be assessed in parallel (Kitchen et al., 2014). We documented the proteomes of purified striatal and hippocampal astrocytes from P30 *Aldh1l1*-EGFP mice (Cahoy et al., 2008; Foo, 2013). The method uses fluorescence-activated cell sorting (FACS) of EGFP-positive cells (Figure S6). Therefore, we validated the isolated cells using microarrays to assess the quality of the samples. For both striatum and hippocampus, the EGFP-positive astrocytes showed high expression of 100 astrocyte markers and low expression of 100 neuronal markers (Figure S7A) and could be considered

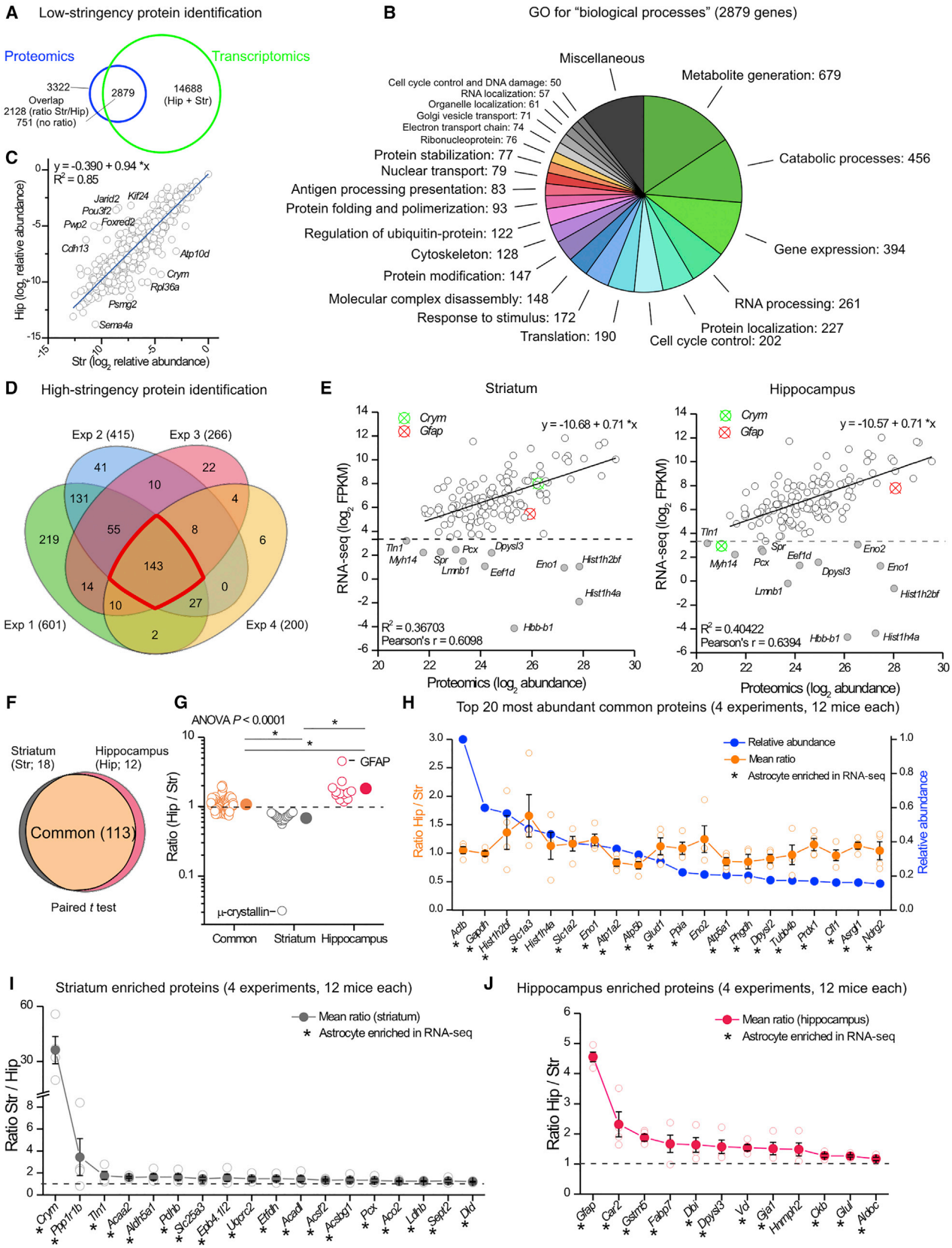

(legend on next page)

astrocytes (Foo, 2013). The expression profiles of astrocytes from striatum and hippocampus were also distinct (Figure S7B). We next quantitatively compared proteomes by independently labeling samples from striata and hippocampi with low- (28 Da) or intermediate- (32 Da) molecular-weight dimethyl labels prior to pooling for liquid chromatography-tandem mass spectrometry (LC-MS/MS) (Boersema et al., 2009). Mass spectrometry data were processed (Figure S7C) and permitted determination of the ratio of low and intermediate dimethyl labels (i.e., relative abundance in striatal and hippocampal astrocytes) and identification of proteins. Many of the top 100 astrocyte markers were strongly represented in the astrocyte proteomic data, but most of the 100 neuronal markers were not (Figure S7D). Thus, our analyses of gene and protein expression in the FACS isolated astrocytes suggests high purity of the cells (Foo, 2013). We cannot completely rule out neuronal contamination in the FACS-isolated material. This is a known limitation of FACS and is also expected, since astrocytes phagocytose neuronal elements (Chung et al., 2015b). Our FACS samples are strongly astrocyte enriched rather than a pure population.

From four biological replicates, we identified 3,509 protein groups corresponding to 3,322 genes (Figure 6A; Data S2). Of these, 2,879 genes were shared with the striatal and hippocampal astrocyte RNA-seq data. Gene ontology analysis showed that most of the shared genes were involved in metabolic processes, gene expression, and protein regulation (Figure 6B). By plotting relative abundance of hippocampal versus striatal proteins ($\log_2$ scale), we determined that 2,128 were detected in both samples (Figure 6C). However, several proteins were more abundant in astrocytes from one or the other brain region (Figure 6C).

To explore robust commonalities and differences between striatal and hippocampal astrocyte proteomes, we performed high-stringency analyses, which resulted in a list of 692 proteins (Data S2). We considered the 143 proteins that were detected in all four experiments (Figure 6D; Data S2). We evaluated the correlation between RNA ($\log_2$ FPKM) and protein ($\log_2$ abundance) levels in both striatum and hippocampus (Figure 6E). There was a clear correlation between the two variables, implying that RNA-seq reflects abundance of most proteins. However, there were notable exceptions, and ~10% of the proteins showed high abundance but low FPKM values (<10) for striatal and hippocampal datasets (Figure 6E). Statistical analyses revealed that out of 143 proteins, the abundance of 113 proteins was not significantly different between striatum and hippocampus (i.e., the common and most abundant proteins) (Data S2). However, 18 proteins in the striatum and 12 proteins in the hippocampus emerged as significantly region enriched (Figure 6F; Data S2). Furthermore, comparison of the ratios for the common, striatal-enriched, and hippocampal-enriched proteins showed that these groups were significantly different (Figure 6G). These data represent the first unbiased identification of proteins that define subpopulations of astrocytes in the brain. The most differentially expressed striatal and hippocampal astrocyte proteins were μ-crystallin (gene: *Crym*) and GFAP (gene: *Gfap*), respectively (Figure 6G), which also had the highest expression among the most differentially expressed transcripts (Figure 4G).

We further assessed the 143 proteins discovered by high-stringency analyses (proteins are referred to by their gene name). We ranked the common proteins by abundance; the top 20 are shown in Figure 6H. Of these, 19 are also astrocyte enriched by RNA-seq and include well-established astrocyte molecules (e.g., *Slc1a3* [GLAST] and *Slc1a2* [GLT1]). A quarter (e.g., *Actb*, *Dpysl2*, *Tubb4b*, and *Cfl1*) are implicated in cytoskeleton remodeling, and some, although highly abundant and common, are of poorly defined function (e.g., *Phgdh*). These top common proteins represent a valuable astrocyte resource (Figure 6H).

Among the 18 striatal-enriched proteins, the most highly enriched was *Crym* (μ-crystallin; Figure 6I). *Crym* binds to thyroid hormone. Another striatal-astrocyte-enriched protein was *Aldh5a1,* which participates in GABA degradation. This appears relevant given that the striatum consists mainly of GABAergic

Figure 6. Striatal and Hippocampal Astrocyte Proteomes

(A) Venn diagram of proteins and genes detected in astrocytes using proteomics and RNA-seq. In total, 3,509 protein groups, corresponding to 3,322 genes, were identified using low-stringency protein identification filters (FDR < 0.01, ΔCn < 0.05). From the 3,322 genes, 2,879 were expressed in astrocytes in transcriptomic data (FPKM > 0.1).

(B) Enrichr gene ontology (GO) analysis for "biological processes" of the 2,879 genes common between proteomics and RNA-seq (functionally related Enrichr GO terms were grouped together).

(C) Of 2,879 genes common between proteomics and RNA-seq, 2,128 were detected in both hippocampus and striatum at the protein level. Scatterplot of relative protein abundance of these 2,128 proteins in hippocampus and striatum shows a high correlation between the two regions but also highlights differentially expressed proteins.

(D) Venn diagram of the number of protein groups identified in the four replicates using high-stringency filters. In total, 143 proteins were found in four replicates.

(E) Scatterplot comparing RNA and protein abundance for the 143 proteins detected in the proteomics high-stringency dataset. Most of the proteins show correlation with RNA levels. However, a subset of proteins (gray filled circles) had high protein levels but low RNA expression (FPKM < 10).

(F) Venn diagram of the common, striatal-enriched, and hippocampal-enriched proteins in the high-stringency dataset. Paired t test analysis was used to determine the differentially expressed proteins between hippocampus and striatum.

(G) Hip/Str ratio distribution of the 143 proteins contained in (F). Ratio of common proteins is significantly different from the proteins enriched in striatum or hippocampus (Kruskal-Wallis ANOVA with *p < 0.05 post hoc Dunn's multiple comparison test). μ-crystallin and GFAP emerge as the most different among these proteins.

(H) Top 20 most abundant common astrocyte proteins.

(I) Striatum-enriched proteins.

(J) Hippocampus-enriched proteins.

In (H)–(J), asterisk (*) indicates genes that were also astrocyte enriched in the RNA-seq data. In these panels, proteins are listed by their gene name. In some cases, the error bars representing SEM are smaller than the symbol used to show the mean.

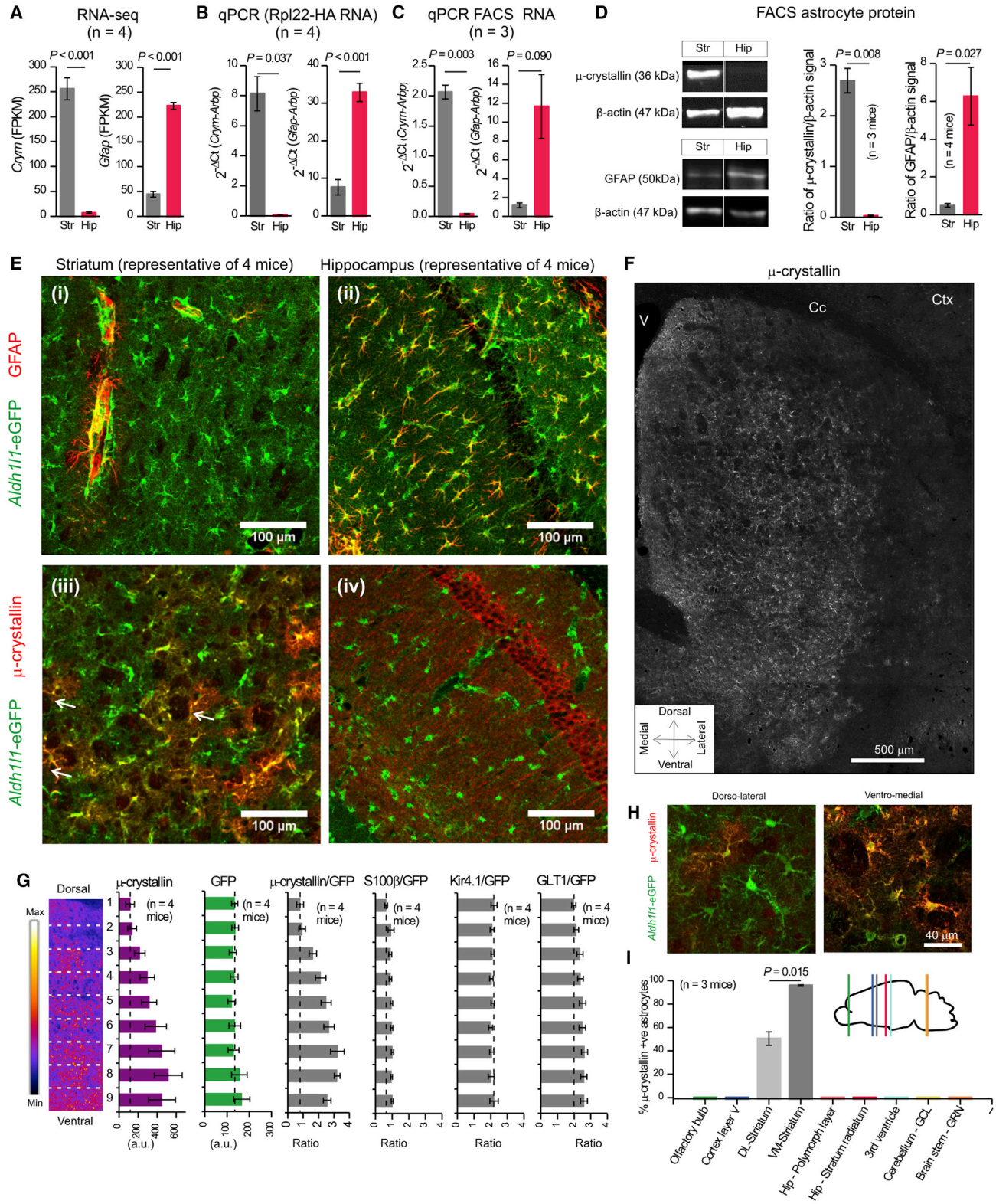

Figure 7. Validating GFAP and μ-Crystallin Expression in Striatal and Hippocampal Astrocytes

(A) RNA-seq FPKM values for *Crym* and *Gfap* in striatum and hippocampus.

(B) qPCR of RNA from P63 *Aldh1l1*-cre/ERT2 × RiboTag mice for *Crym* and *Gfap* in the striatum and hippocampus.

(legend continued on next page)

MSNs. In hippocampal astrocytes, 12 proteins were significantly enriched (Figure 6J), including *Gfap*, an intermediate filament, and *Car2*, a carbonic anhydrase. Other notable proteins higher in hippocampus were *Gja1* (Connexin 43) and glutamine synthetase *Glul*. The higher levels of Connexin 43 in the hippocampus might be related to the greater degree of CBX-resistant gap-junction coupling in that region (Figures 1I and 1J).

The proteomic data are available as Data S2, at the Proteome Exchange Consortium via PRIDE (PRIDE: PXD005852), and at http://astrocyternaseq.org.

Validating the Top Striatal and Hippocampal Astrocyte-Enriched Genes

Proteomics and RNA-seq revealed μ-crystallin (*Crym*) and GFAP (*Gfap*) as abundant and differentially expressed between striatal and hippocampal astrocytes (Figures 6I, 6J, and 7A). To validate these, we performed qPCR for *Crym* and *Gfap* with astrocyte RNA obtained from P63 *Aldh1l1*-cre/ERT2 × Rpl22HA mice (Figure 7B) and P30 *Aldh1l1*-EGFP astrocytes isolated by FACS (Figure 7C). With both sets of samples, we found that RNA levels of *Crym* were significantly higher in striatal astrocytes but undetectable in hippocampal astrocytes. Similarly, *Gfap* RNA was enriched in hippocampal astrocytes in relation to striatal astrocytes. The data were further validated by western blot of FACS-isolated astrocytes (Figure 7D) and immunohistochemistry (IHC) in *Aldh1l1*-EGFP reporter mice (Figure 7E). Only 7% ± 2% of astrocytes in the d.l. striatum showed GFAP staining (1,314 cells examined from n = 4 mice; Figure 7Ei), whereas GFAP was expressed in all hippocampal s.r. astrocytes (620 cells examined from n = 4 mice; Figure 7Eii). Furthermore, no immunostaining was observed for μ-crystallin in hippocampal astrocytes (n = 3 mice), although it was found in pyramidal neurons (Figure 7Eiv). In the d.l. striatum, μ-crystallin immunostaining was obvious within 50% ± 6% of astrocytes (Figure 7Eiii, n = 3 mice; Figure S8A). We also observed that μ-crystallin-positive astrocytes displayed a gradient in the striatum; their density increased along the dorsal-to-ventral axis, peaking in the ventromedial region (Figure 7F–7H). This gradient was not shared with EGFP (from *Aldh1l1*-EGFP mice), S100β, Kir4.1, or GLT1 (Figure 7G). This provides strong evidence that the density of astrocytes is equivalent throughout the striatum but that μ-crystallin displays a gradient. Furthermore, we evaluated μ-crystallin expression in *Aldh1l1*-EGFP-positive astrocytes broadly in the brain and found it only within striatal astrocytes (Figure 7I). μ-crystallin was not reliably detected at P0, but the differences between striatum and hippocampus, and within the striatum, were observed at P7 and P30 (Figure S8B).

Assessing Ca^{2+}-Dependent Glutamate Exocytosis from Astrocytes

Based on RNA-seq and proteomic data (Figures 4, 5, and 6; Data S1 and S2), as well as experiments showing differences in signaling and morphology between striatal and hippocampal astrocytes (Figures 1, 2, and 3), we explored if Ca^{2+}-dependent glutamate exocytosis also differed. Recent studies suggest that hippocampal and striatal astrocytes from young rodents display Ca^{2+}-dependent glutamate exocytosis (Araque et al., 2000, 2014; D'Ascenzo et al., 2007; Martín et al., 2015; Navarrete and Araque, 2008; Perea and Araque, 2007).

Figure 8A plots striatal and hippocampal astrocyte FPKM values for genes involved in Ca^{2+}-dependent exocytosis (four synaptobrevins, four SNAPs, four syntaxins, five synaptotagmins, four complexins, four syntaxin-binding proteins, and three vesicular glutamate transporters [vGluts]). As a metric to assess these data, we plotted FPKM values for known astrocyte markers, neuron markers, and housekeeping genes (Figure 8A, n = 4). The stars in Figure 8A highlight FPKM values that were significantly greater than 10 ($p < 0.05$; one-sample t test). Notably, striatal and hippocampal astrocytes express *Vamp2*, *Vamp3*, *Vamp4*, *Snap25*, *Snap29*, *Snap47*, *Stx4a*, *Syt11, Cplx2*, *Stxbp3a*, and *Stxbp4* mRNAs above this threshold (Figure 8A). However, neither striatal nor hippocampal astrocytes expressed significant RNA for vGluts or Ca^{2+}-sensitive synaptotagmins. Synaptotagmin 11 (*Syt11*) was significantly expressed in our data and in a previous study (Zhang et al., 2014), but it does not bind Ca^{2+} due to the absence of essential aspartates (Pang and Südhof, 2010; von Poser et al., 1997). Of the genes related to Ca^{2+}-dependent exocytosis, only *Vamp2* was found in the high-stringency proteomic data, although several were found in the low-stringency dataset (Data S2). Furthermore, although we readily observed vesicles in 138 striatal and 139 hippocampal synapses (Figure 3), we observed no astrocyte processes that contained structures akin to neurotransmitter vesicles at the same synapses. Hence, the astrocyte data indicate membrane-traffic-related gene expression but show little evidence for minimal requirements for Ca^{2+}-dependent glutamate exocytosis (i.e., for a Ca^{2+} sensor or a vGlut).

We next sought to measure Gq GPCR-mediated glutamate release from d.l. striatal and hippocampal CA1 s.r. astrocytes using the genetically encoded glutamate sensor iGluSnFR, which has requisite kinetics and sensitivity (Haustein et al., 2014; Jiang et al., 2016; Marvin et al., 2013). We targeted iGluSnFR to astrocyte extracellular surfaces and co-expressed it with hM3D DREADDs (Figure 8B). We found no evidence for spontaneous iGluSnFR fluorescence increases (flashes) and no

(C) qPCR of mRNA extracted from P30 FACS astrocytes for *Crym* and *Gfap* in the striatum and hippocampus.
(D) Western blot for μ-crystallin and GFAP from striatal and hippocampal FACS astrocytes, with quantification normalized to β-actin.
(E) IHC of GFAP and μ-crystallin in the d.l. striatum and hippocampus CA1 s.r. of *Aldh1l1*-eGFP mice. In the striatum, a high proportion of astrocytes stain for μ-crystallin (arrows in Eiii). The spectrally separated images are shown in Figure S8A.
(F) μ-Crystallin immunostaining in striatum showing its spatial gradient (V, ventricle; Cc, corpus callosum; Ctx, cortex).
(G) Quantification of μ-crystallin, S100β, Kir4.1 and GLT1 signal intensity in *Aldh1l1*-EGFP mice along the dorsoventral axis of the striatum. The signal was normalized to GFP signal.
(H) μ-Crystallin immunostaining in the d.l. and ventromedial striatum of *Aldh1l1*-EGFP mice.
(I) Quantification of μ-crystallin-positive astrocytes in nine brain areas.
Average data are shown as mean ± SEM.

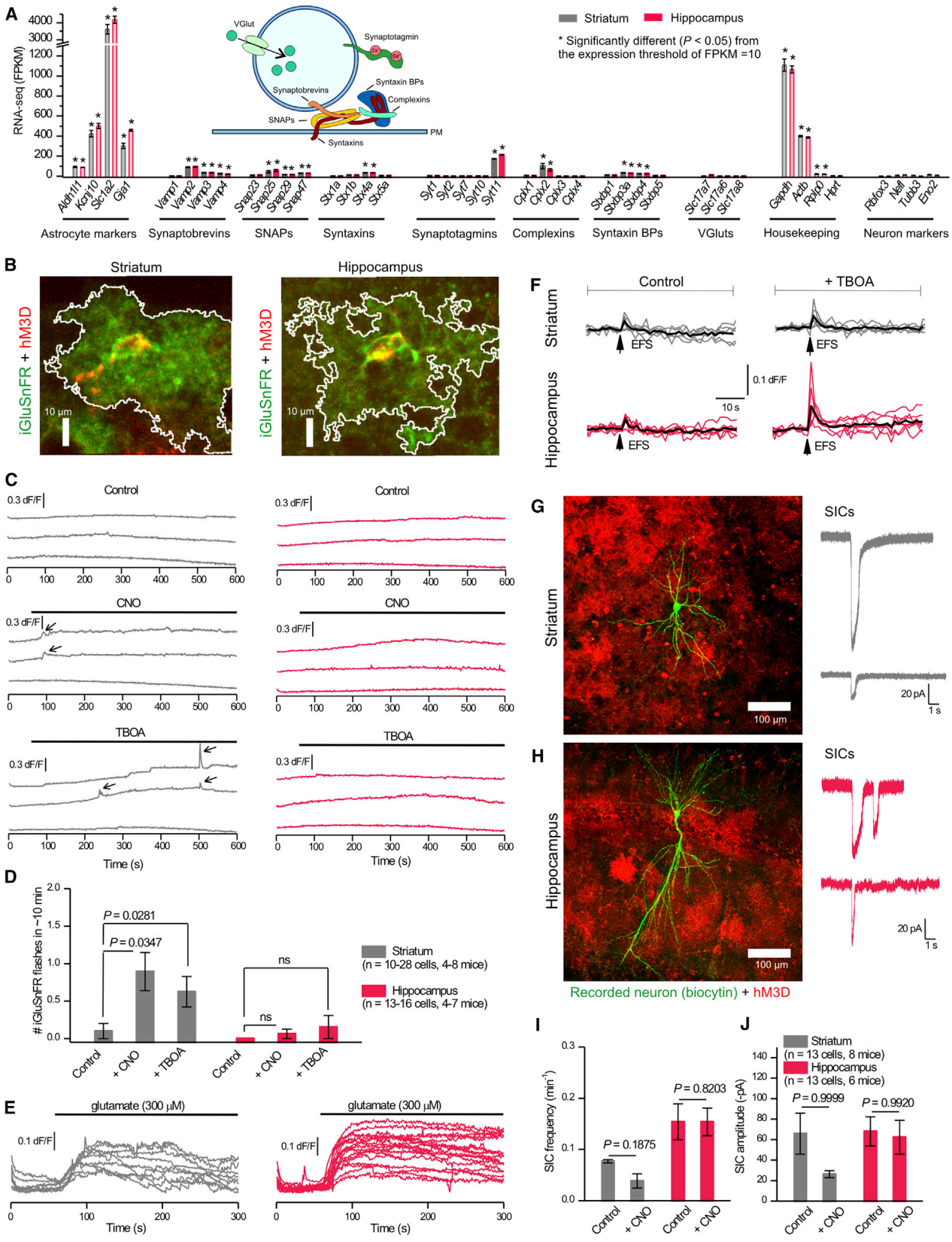

(legend on next page)

strong evidence for CNO-evoked iGluSnFR flashes, even though CNO activation of hM3D always increased astrocyte Ca^{2+} levels (Figures 2E–2H and 8B–8D). We note that there was a statistically significant increase in iGluSnFR flashes from striatal astrocytes, but this corresponds to only one iGluSnFR flash every 10 min (Figure 8D). It is also comparable to that observed by blocking GLT1 with TBOA and was not observed in hippocampal astrocytes (Figure 8D). CNO also failed to cause any increase in basal iGluSnFR fluorescence. Striatal astrocyte basal iGluSnFR fluorescence was 534 ± 41 arbitrary units (a.u.) in control and 348 ± 21 a.u. with CNO. Hippocampal astrocyte basal iGluSnFR fluorescence was 392 ± 41 a.u. in control and 274 ± 17 a.u. with CNO. However, both striatal and hippocampal astrocytes responded to exogenous glutamate (Figure 8E), and EFS of glutamatergic inputs with four APs (Figure 8F) resulted in significant astrocyte iGluSnFR signals. Moreover, application of 1 μM (3S)-3-[[3-[[4-(trifluoromethyl)benzoyl]amino]phenyl]methoxy]-L-aspartic acid (TBOA) to block GLT1 significantly increased EFS-evoked iGluSnFR signals onto hippocampal ($p = 0.04324$), but not striatal astrocytes (Figure 8F; $p = 0.27499$). With these controls, we feel confident that we would have detected comparable glutamate release from astrocytes had it occurred. Furthermore, in young mice, astrocyte glutamate release may activate neuronal extrasynaptic NMDA receptors to evoke slow inward currents (SICs) (Shigetomi et al., 2008). We thus also recorded from d.l. striatal MSNs and hippocampal CA1 pyramidal neurons in the vicinity of astrocytes expressing hM3D DREADDs and applied CNO (Figures 8G and 8H). We could readily measure SICs in both MSNs and pyramidal neurons, but we failed to measure significant CNO-evoked increases in their frequency or amplitude (Figures 8I and 8J). Overall, our data are broadly consistent with past evaluations with purified astrocytes (Foo et al., 2011) and argue against Ca^{2+}-dependent glutamate exocytosis as a core or robust astrocyte attribute.

DISCUSSION

Astrocytes have been considered a homogeneous glue-like cell. However, astrocyte diversity has been widely invoked recently to explain the plethora of physiological processes that astrocytes participate in (Ben Haim and Rowitch, 2017; Khakh and Sofroniew, 2015; Zhang and Barres, 2010). We used several methods to assess astrocyte similarity or diversity in two distinct neural circuits mediating distinct functions and largely comprising distinct neuron types. Our data show that astrocytes in the hippocampus and striatum share many similarities but are distinct by several metrics at functional, morphological, and molecular levels of evaluation. Our data provide proof for neural-circuit-specialized astrocytes in the adult brain, extending work from the spinal cord (Molofsky et al., 2014).

At a functional level, striatal and hippocampal astrocytes differed significantly in the size of Ba^{2+}-sensitive K^+ currents, gap-junctional coupling, and spontaneous, electrically evoked and GPCR-mediated Ca^{2+} signals. They also differed in the effect of TBOA on electrically evoked glutamate signals. Morphologically, striatal, and hippocampal astrocytes differed in their territory size, number of neuronal somata they contacted, the numbers of synapses within a territory, and the proximity of astrocyte processes to excitatory synapses. At a molecular level, they differed significantly in their transcriptomes and proteomes.

The adult RNA-seq and proteomic data provide resources to explore astrocyte functions in hypothesis-driven experiments employing genetic and functional approaches. For example, the list of the 20 most abundant astrocyte proteins shared between striatal and hippocampal astrocytes reveals several whose functions are unclear. In addition, our data confirm in adults at the protein and RNA levels many known critical astrocyte functions, such as neurotransmitter clearance, K^+ homeostasis, and roles in synapse formation and pruning. In that regard, we found that Ba^{2+}-sensitive K^+ currents were larger in hippocampal astrocytes. However, *Kcnj10* FPKM values and the hippocampal/striatal protein ratio were not significantly different, although both trended higher in the hippocampus by ~10%–15%. Hence, Kir4.1 expression differences do not satisfactorily explain why hippocampal astrocytes displayed larger Ba^{2+}-sensitive currents, although it is possible that the relationships among RNA, protein, and measurement of function are complex. However, evaluation of all K^+ channel genes identified several differences and Kir5.1 (*Kcnj16*) as significantly hippocampal astrocyte enriched relative to striatum by 3-fold; this may underlie the larger Ba^{2+}-sensitive currents. Furthermore, the Ba^{2+}-resistant currents could be partly due to SK and 2P K^+ channels (*Kcnn2*, *Kcnn3*, and *Kcnk1*). Thus, the

Figure 8. Assessing Striatal and Hippocampal Astrocyte Ca^{2+}-Evoked Glutamate Exocytosis

(A) Expression of known exocytosis genes in striatal and hippocampal RNA-seq data (n = 4) were compared against known cell-specific markers and housekeeping genes. One-sample t tests were run against the threshold of 10 FPKM. Inset: schematic of the machinery involved in glutamate exocytosis.

(B) Example images of iGluSnFR (green) coexpressed with Gq-coupled DREADD hM3D (red) in astrocytes. White line indicates area analyzed for iGluSnFR fluorescence.

(C) Example traces from d.l. striatal (gray) and hippocampal CA1 s.r. (red) astrocytes of iGluSnFR dF/F in control conditions, with application of CNO (1 μM) to increase astrocyte Ca^{2+} or with application of 1 μM (3S)-3-[[3-[[4-(trifluoromethyl)benzoyl]amino]phenyl]methoxy]-L-aspartic acid (TBOA) to block glutamate transporters. iGluSnFR flashes are indicated with arrows.

(D) The number of iGluSnFR flashes compared among control, +CNO, and +TBOA.

(E) iGluSnFR traces show increased fluorescence with bath application of 300 μM glutamate (1 μM TBOA; n = 12 cells per region from four mice).

(F) EFS-evoked (four APs at 10 Hz) iGluSnFR signals recorded from d.l. striatal and hippocampal CA1 s.r. astrocytes under control conditions and in the presence of TBOA (n = 6 and 7 fields of view from three mice each).

(G) Left: a recorded striatal MSN as visualized by biocytin (green) surrounded by an hM3D-expressing astrocyte (red mCherry signal). Right: example traces from neurons in voltage clamp shows slow inward currents (SICs) at −70 mV.

(H) As in (G), but for hippocampal CA1 pyramidal neurons.

(I and J) The frequency (I) and amplitude (J) of SICs per minute in 10 min of control conditions and 10 min with CNO. 0.25 μM TTX was present in all experiments. Average data are shown as mean ± SEM.

RNA and protein analyses provide several new hypotheses to explore the large resting K^+ conductance of astrocytes (Nwaobi et al., 2016). Irrespectively, lower Ba^{2+}-sensitive currents, CBX-sensitive gap-junctional coupling, and glutamine synthetase levels (Data S1; Figures 6I and 6J) in striatal astrocytes may be consistent with the fact the striatum comprises predominantly GABAergic neurons with hyperpolarized membrane potentials. Presumably, they have a lower requirement for K^+ buffering, K^+ dissipation, and glutamate recycling.

We examined the potential for Ca^{2+}-dependent glutamate exocytosis from adult astrocytes (Bazargani and Attwell, 2015). We restrict our discussion to recent work on striatal and hippocampal slices (Martín et al., 2015; Navarrete and Araque, 2008; Perea and Araque, 2007). We found little evidence for the presence of a core molecular machinery within adult astrocytes to support Ca^{2+}-dependent glutamate exocytosis. Furthermore, although we could evoke large-amplitude astrocyte Ca^{2+} elevations and image exogenous and neuronal glutamate release onto astrocytes, we found no evidence for Ca^{2+}-dependent glutamate release from astrocytes onto astrocytes and nearby neurons in adult mice. This contrasts with some, but not all, aspects of our past work on young mice (Shigetomi et al., 2008). While we do not negate observations on the possible importance of astrocyte Ca^{2+}-dependent glutamate release for striatal and hippocampal function, we suggest the need for caution in drawing interpretations for adult neural circuits, behavior, and disease until compelling evidence is obtained from mature neural circuits. Our evaluations failed to find such evidence in adult mice and support the view that adult astrocytes differ in physiologically significant ways from those in younger mice (Srinivasan et al., 2016; Sun et al., 2013).

The top striatal- or hippocampal-astrocyte-enriched genes and proteins identified by RNA-seq and LC-MS/MS were validated by qPCR, immunostaining, and western blot analyses. The finding that GFAP was low in striatal astrocytes across all our measurements emphasizes the limitations of GFAP and speaks to the greater utility of the *Aldh1l1* locus. To our knowledge, the discovery that μ-crystallin is specific for striatal astrocytes provides the first molecular marker that defines a region-specific astrocyte population. Moreover, striatal astrocytes are known to be altered in Huntington's disease (HD) (Khakh et al., 2017), and μ-crystallin levels decrease in humans and mouse models of HD (Francelle et al., 2015). Interestingly, six of the top 40 striatal enriched astrocyte genes are histones, which is consistent with the GSEA results that chromosome-structure-related gene sets were striatal enriched. The striatal enrichment of cell-cycle- and mitosis-related genes in astrocytes may indicate that striatal astrocytes are poised to respond to stimuli with proliferation, for example as may occur in the context of striatal diseases such as HD. Our database resources, mouse models (Srinivasan et al., 2016), AAVs, and other reagents can now be used for detailed exploration of striatal astrocytes.

μ-Crystallin is interesting from another perspective. It displayed a clearly significant gradient of expression in the striatum and was patchy in the d.l. region. This provides evidence that even locally arranged astrocytes within a neural circuit (dorsal versus ventral striatum) or even more locally (i.e., neighboring astrocytes in the d.l. region) may be heterogeneous. However, we suggest that proof for the existence of such highly local heterogeneity should be based on candid assessment of cell markers, gene expression, protein expression, physiology, and morphology. Additional technical advances are necessary to deploy the combination of such methods to study locally intermingled astrocytes. Our data showing that RNA and protein levels are not necessarily directly correlated in all cases echoes previous work (Kitchen et al., 2014) and provides an impetus to assess local diversity with multiple approaches.

In summary, optical, anatomical, electrophysiological, transcriptomic, and proteomic approaches were deployed to explore astrocyte similarities and differences in two neural circuits. Candid evaluation of the data across ten approaches provided direct evidence for astrocyte diversity and provided resources to explore astrocytes across the brain. Future studies could explore how astrocyte diversity between the hippocampus and striatum arises: Are the differences intrinsic, or do they arise due to the local environment of the circuit? Do hippocampal and striatal astrocytes come from different stem cells or from a common origin that adopts distinct phenotypes? Finally, by providing evidence for neural-circuit-specialized astrocytes in the adult brain, our data portend their therapeutic exploitation for the modulation of neural-circuit-specific disease states.

STAR★METHODS

Detailed methods are provided in the online version of this paper and include the following:

- KEY RESOURCES TABLE
- CONTACT FOR REAGENT AND RESOURCE SHARING
- EXPERIMENTAL MODEL AND SUBJECT DETAILS
  - Mouse models
- METHOD DETAILS
  - Experimental design
  - Stereotaxic microinjections of adeno-associated viruses
  - In vivo activation of HM4D
  - Immunohistochemistry (IHC)
  - Acute brain slice preparation for imaging and electrophysiology
  - Electrophysiological recording and assessment of dye coupling in brain slices
  - Intracellular Ca^{2+} and cell surface glutamate imaging
  - Brain tissue clearing
  - Astrocyte intracellular Lucifer yellow iontophoresis
  - Electron Microscopy
  - RNA-seq determination of striatal and hippocampal astrocyte transcriptomes and analyses
  - RNA and protein extraction from astrocytes isolated by FACS
  - Microarrays of FACS astrocytes
  - Mass spectrometry based proteomics
  - qPCR experiments
  - Western blot analyses
- QUANTIFICATION AND STATISTICAL ANALYSIS
- DATA AND SOFTWARE AVAILABILITY
- ADDITIONAL RESOURCES

SUPPLEMENTAL INFORMATION

Supplemental Information contains eight figures, two tables, four movies, and two data files and can be found with this article online at http://dx.doi.org/10.1016/j.neuron.2017.06.029.

AUTHOR CONTRIBUTIONS

H.C. did the serial block-face electron microscopy, stereotaxic injections, RNA-seq, imaging, and in vivo experiments. B.D.-C. performed FACS and analyzed proteomic data. H.C. and B.D.-C. performed immunohistochemistry, western blotting, and RNA-seq analyses. E.S. performed some imaging. P.S.R. performed brain clearing. X.Y. and J.C.O. performed gene cloning. E.M. and T.M.V. helped guide and troubleshoot the proteomic work. B.D.-C., W.C., and J.P.W. were responsible for sample preparation with isotope coding and mass spectrometer operation; W.C. and J.P.W. also guided B.D.-C. with LC-MS/MS data analyses. G.C. helped analyze the RNA-seq and microarray data. H.C. and B.S.K. performed electrophysiology. H.C., B.D.-C., and B.S.K. analyzed data. B.S.K. conceived the study, directed the experiments, and assembled the figures with help from H.C. and B.D.-C. B.S.K. wrote the paper with help from H.C. and B.D.-C. All authors contributed to the final version of the manuscript.

ACKNOWLEDGMENTS

This work was supported by the NIH (MH099559 and MH104069 to B.S.K.). We thank the NINDS Informatics Center for Neurogenetics and Neurogenomics at UCLA (P30 NS062691), the IDDRC (U54HD087101), and Fuying Gao for assistance with gene expression analysis. We thank Sandeep Deverasetty for developing the Astrocyte RNA-seq Explorer website. H.C. was supported by an NIH F30 Training Fellowship (MH106197). E.S. was supported by JSPS KAKENHI (JP15KK0340). E.M. was supported by an American Heart Association predoctoral fellowship (13PRE14430015). X.Y. was supported by an American Heart Association postdoctoral fellowship (16POST27260256). J.P.W. acknowledges support from the UCSD/UCLA NIDDK Diabetes Research Center (P30 DK063491). J.C.O. thanks the NIH T32 Neural Microcircuits Training Grant (NS058280). We thank Michael V. Sofroniew for providing access to equipment, Kalyanam Shivkumar for mentoring P.S.R., Chen Cheng for discussions about RNA-seq, Dr. Amy Gleichman for providing tips on IP, and Alexander Reeves for help with cloning at the early stages. We also thank the UCLA Clinical Microarray Core and the UCLA Neuroscience Genomics Core. Flow cytometry was performed in the UCLA Jonsson Comprehensive Cancer Center (JCCC) and Center for AIDS Research Flow Cytometry Core Facility. We thank the Gradinaru Laboratory at Caltech for help with tissue clearing and confocal imaging of our samples through the Beckman Institute for the Resource Center on CLARITY, Optogenetics, and Vector Engineering for technology development and broad dissemination (http://www.beckmaninstitute.caltech.edu/clover.shtml). H.C. and P.S.R. belong to the Medical Scientist Training Program at UCLA. We thank Drs. Bazbek Davletov (Sheffield, UK) and Rahul Srinivasan (Texas A&M) for their comments on the manuscript.

Received: February 7, 2017
Revised: May 14, 2017
Accepted: June 16, 2017
Published: July 13, 2017

REFERENCES

Anders, S., Pyl, P.T., and Huber, W. (2015). HTSeq: a Python framework to work with high-throughput sequencing data. Bioinformatics *31*, 166–169.

Araque, A., Li, N., Doyle, R.T., and Haydon, P.G. (2000). SNARE protein-dependent glutamate release from astrocytes. J. Neurosci. *20*, 666–673.

Araque, A., Carmignoto, G., Haydon, P.G., Oliet, S.H., Robitaille, R., and Volterra, A. (2014). Gliotransmitters travel in time and space. Neuron *81*, 728–739.

Arellano, J.I., Benavides-Piccione, R., Defelipe, J., and Yuste, R. (2007). Ultrastructure of dendritic spines: correlation between synaptic and spine morphologies. Front. Neurosci. *1*, 131–143.

Bazargani, N., and Attwell, D. (2015). Astrocyte calcium signalling: the third wave. Nat. Neurosci. *19*, 182–189.

Bello-Medina, P.C., Flores, G., Quirarte, G.L., McGaugh, J.L., and Prado Alcalá, R.A. (2016). Mushroom spine dynamics in medium spiny neurons of dorsal striatum associated with memory of moderate and intense training. Proc. Natl. Acad. Sci. USA *113*, E6516–E6525.

Ben Haim, L., and Rowitch, D.H. (2017). Functional diversity of astrocytes in neural circuit regulation. Nat. Rev. Neurosci. *18*, 31–41.

Boersema, P.J., Raijmakers, R., Lemeer, S., Mohammed, S., and Heck, A.J. (2009). Multiplex peptide stable isotope dimethyl labeling for quantitative proteomics. Nat. Protoc. *4*, 484–494.

Bushong, E.A., Martone, M.E., Jones, Y.Z., and Ellisman, M.H. (2002). Protoplasmic astrocytes in CA1 stratum radiatum occupy separate anatomical domains. J. Neurosci. *22*, 183–192.

Cahoy, J.D., Emery, B., Kaushal, A., Foo, L.C., Zamanian, J.L., Christopherson, K.S., Xing, Y., Lubischer, J.L., Krieg, P.A., Krupenko, S.A., et al. (2008). A transcriptome database for astrocytes, neurons, and oligodendrocytes: a new resource for understanding brain development and function. J. Neurosci. *28*, 264–278.

Chung, W.-S., Welsh, C.A., Barres, B.A., and Stevens, B. (2015a). Do glia drive synaptic and cognitive impairment in disease? Nat. Neurosci. *18*, 1539–1545.

Chung, W.S., Allen, N.J., and Eroglu, C. (2015b). Astrocytes control synapse formation, function, and elimination. Cold Spring Harb. Perspect. Biol. *7*, a020370.

Cui, Q., Pitt, J.E., Pamukcu, A., Poulin, J.F., Mabrouk, O.S., Fiske, M.P., Fan, I.B., Augustine, E.C., Young, K.A., Kennedy, R.T., et al. (2016). Blunted mGluR activation disinhibits striatopallidal transmission in Parkinsonian mice. Cell Rep. *17*, 2431–2444.

D'Ascenzo, M., Fellin, T., Terunuma, M., Revilla-Sanchez, R., Meaney, D.F., Auberson, Y.P., Moss, S.J., and Haydon, P.G. (2007). mGluR5 stimulates gliotransmission in the nucleus accumbens. Proc. Natl. Acad. Sci. USA *104*, 1995–2000.

Fiala, J.C. (2005). Reconstruct: a free editor for serial section microscopy. J. Microsc. *218*, 52–61.

Fiala, J.C., Kirov, S.A., Feinberg, M.D., Petrak, L.J., George, P., Goddard, C.A., and Harris, K.M. (2003). Timing of neuronal and glial ultrastructure disruption during brain slice preparation and recovery in vitro. J. Comp. Neurol. *465*, 90–103.

Foo, L.C. (2013). Purification of astrocytes from transgenic rodents by fluorescence-activated cell sorting. Cold Spring Harb. Protoc. *2013*, 551–560.

Foo, L.C., Allen, N.J., Bushong, E.A., Ventura, P.B., Chung, W.S., Zhou, L., Cahoy, J.D., Daneman, R., Zong, H., Ellisman, M.H., and Barres, B.A. (2011). Development of a method for the purification and culture of rodent astrocytes. Neuron *71*, 799–811.

Francelle, L., Galvan, L., Gaillard, M.C., Guillermier, M., Houitte, D., Bonvento, G., Petit, F., Jan, C., Dufour, N., Hantraye, P., et al. (2015). Loss of the thyroid hormone-binding protein Crym renders striatal neurons more vulnerable to mutant huntingtin in Huntington's disease. Hum. Mol. Genet. *24*, 1563–1573.

Graybiel, A.M. (2008). Habits, rituals, and the evaluative brain. Annu. Rev. Neurosci. *31*, 359–387.

Hama, H., Hioki, H., Namiki, K., Hoshida, T., Kurokawa, H., Ishidate, F., Kaneko, T., Akagi, T., Saito, T., Saido, T., and Miyawaki, A. (2015). ScaleS: an optical clearing palette for biological imaging. Nat. Neurosci. *18*, 1518–1529.

Harris, K.M., Jensen, F.E., and Tsao, B. (1992). Three-dimensional structure of dendritic spines and synapses in rat hippocampus (CA1) at postnatal day 15 and adult ages: implications for the maturation of synaptic physiology and long-term potentiation. J. Neurosci. *12*, 2685–2705.

Haustein, M.D., Kracun, S., Lu, X.H., Shih, T., Jackson-Weaver, O., Tong, X., Xu, J., Yang, X.W., O'Dell, T.J., Marvin, J.S., et al. (2014). Conditions and

constraints for astrocyte calcium signaling in the hippocampal mossy fiber pathway. Neuron *82*, 413–429.

Ingham, C.A., Hood, S.H., Taggart, P., and Arbuthnott, G.W. (1998). Plasticity of synapses in the rat neostriatum after unilateral lesion of the nigrostriatal dopaminergic pathway. J. Neurosci. *18*, 4732–4743.

Jiang, R., Haustein, M.D., Sofroniew, M.V., and Khakh, B.S. (2014). Imaging intracellular Ca^{2+} signals in striatal astrocytes from adult mice using genetically-encoded calcium indicators. J. Vis. Exp. *93*, e51972.

Jiang, R., Diaz-Castro, B., Looger, L.L., and Khakh, B.S. (2016). Dysfunctional calcium and glutamate signaling in striatal astrocytes from Huntington's disease model mice. J. Neurosci. *36*, 3453–3470.

John Lin, C.C., Yu, K., Hatcher, A., Huang, T.W., Lee, H.K., Carlson, J., Weston, M.C., Chen, F., Zhang, Y., Zhu, W., et al. (2017). Identification of diverse astrocyte populations and their malignant analogs. Nat. Neurosci. *20*, 396–405.

Kepecs, A., and Fishell, G. (2014). Interneuron cell types are fit to function. Nature *505*, 318–326.

Khakh, B.S., and Sofroniew, M.V. (2015). Diversity of astrocyte functions and phenotypes in neural circuits. Nat. Neurosci. *18*, 942–952.

Khakh, B.S., Beaumont, V., Cachope, R., Munoz-Sanjuan, I., Goldman, S.A., and Grantyn, R. (2017). Unravelling and exploiting astrocyte dysfunction in Huntington's disease. Trends Neurosci. *40*, 422–437.

Kitchen, R.R., Rozowsky, J.S., Gerstein, M.B., and Nairn, A.C. (2014). Decoding neuroproteomics: integrating the genome, translatome and functional anatomy. Nat. Neurosci. *17*, 1491–1499.

Kuleshov, M.V., Jones, M.R., Rouillard, A.D., Fernandez, N.F., Duan, Q., Wang, Z., Koplev, S., Jenkins, S.L., Jagodnik, K.M., Lachmann, A., et al. (2016). Enrichr: a comprehensive gene set enrichment analysis web server 2016 update. Nucleic Acids Res. *44*, W90–W97.

Law, C.W., Chen, Y., Shi, W., and Smyth, G.K. (2014). voom: precision weights unlock linear model analysis tools for RNA-seq read counts. Genome Biol. *15*, R29.

Liddelow, S.A., Guttenplan, K.A., Clarke, L.E., Bennett, F.C., Bohlen, C.J., Schirmer, L., Bennett, M.L., Münch, A.E., Chung, W.-S., Peterson, T.C., et al. (2017). Neurotoxic reactive astrocytes are induced by activated microglia. Nature *541*, 481–487.

Martín, R., Bajo-Grañeras, R., Moratalla, R., Perea, G., and Araque, A. (2015). Circuit-specific signaling in astrocyte-neuron networks in basal ganglia pathways. Science *349*, 730–734.

Marvin, J.S., Borghuis, B.G., Tian, L., Cichon, J., Harnett, M.T., Akerboom, J., Gordus, A., Renninger, S.L., Chen, T.W., Bargmann, C.I., et al. (2013). An optimized fluorescent probe for visualizing glutamate neurotransmission. Nat. Methods *10*, 162–170.

Molofsky, A.V., Kelley, K.W., Tsai, H.H., Redmond, S.A., Chang, S.M., Madireddy, L., Chan, J.R., Baranzini, S.E., Ullian, E.M., and Rowitch, D.H. (2014). Astrocyte-encoded positional cues maintain sensorimotor circuit integrity. Nature *509*, 189–194.

Navarrete, M., and Araque, A. (2008). Endocannabinoids mediate neuron-astrocyte communication. Neuron *57*, 883–893.

Nwaobi, S.E., Cuddapah, V.A., Patterson, K.C., Randolph, A.C., and Olsen, M.L. (2016). The role of glial-specific Kir4.1 in normal and pathological states of the CNS. Acta Neuropathol. *132*, 1–21.

Pang, Z.P., and Südhof, T.C. (2010). Cell biology of Ca2+-triggered exocytosis. Curr. Opin. Cell Biol. *22*, 496–505.

Perea, G., and Araque, A. (2007). Astrocytes potentiate transmitter release at single hippocampal synapses. Science *317*, 1083–1086.

RCoreTeam (2016). R: A Language and Environment for Statistical Computing. R Foundation for Statistical Computing.

Roth, B.L. (2016). DREADDs for neuroscientists. Neuron *89*, 683–694.

Rungta, R.L., Bernier, L.P., Dissing-Olesen, L., Groten, C.J., LeDue, J.M., Ko, R., Drissler, S., and MacVicar, B.A. (2016). Ca(2+) transients in astrocyte fine processes occur via Ca(2+) influx in the adult mouse hippocampus. Glia *64*, 2093–2103.

Sanz, E., Yang, L., Su, T., Morris, D.R., McKnight, G.S., and Amieux, P.S. (2009). Cell-type-specific isolation of ribosome-associated mRNA from complex tissues. Proc. Natl. Acad. Sci. USA *106*, 13939–13944.

Shigetomi, E., Bowser, D.N., Sofroniew, M.V., and Khakh, B.S. (2008). Two forms of astrocyte calcium excitability have distinct effects on NMDA receptor-mediated slow inward currents in pyramidal neurons. J. Neurosci. *28*, 6659–6663.

Shigetomi, E., Bushong, E.A., Haustein, M.D., Tong, X., Jackson-Weaver, O., Kracun, S., Xu, J., Sofroniew, M.V., Ellisman, M.H., and Khakh, B.S. (2013). Imaging calcium microdomains within entire astrocyte territories and endfeet with GCaMPs expressed using adeno-associated viruses. J. Gen. Physiol. *141*, 633–647.

Shigetomi, E., Patel, S., and Khakh, B.S. (2016). Probing the complexities of astrocyte calcium signaling. Trends Cell Biol. *26*, 300–312.

Soreq, L., Rose, J., Soreq, E., Hardy, J., Trabzuni, D., Cookson, M.R., Smith, C., Ryten, M., Patani, R., and Ule, J.; UK Brain Expression Consortium; North American Brain Expression Consortium (2017). Major shifts in glial regional identity are a transcriptional hallmark of human brain aging. Cell Rep. *18*, 557–570.

Spruston, N., and McBain, C. (2007). Structural and functional properties of hippocampal neurons. In The Hippocampus Book, P. Andersen, R. Morris, D. Amaral, T. Bliss, and J. O'Keefe, eds. (Oxford University Press), pp. 133–201.

Srinivasan, R., Huang, B.S., Venugopal, S., Johnston, A.D., Chai, H., Zeng, H., Golshani, P., and Khakh, B.S. (2015). Ca(2+) signaling in astrocytes from Ip3r2(-/-) mice in brain slices and during startle responses in vivo. Nat. Neurosci. *18*, 708–717.

Srinivasan, R., Lu, T.-Y., Chai, H., Xu, J., Huang, B.S., Golshani, P., Coppola, G., and Khakh, B.S. (2016). New transgenic mouse lines for selectively targeting astrocytes and studying calcium signals in astrocyte processes in situ and in vivo. Neuron *92*, 1181–1195.

Sun, W., McConnell, E., Pare, J.F., Xu, Q., Chen, M., Peng, W., Lovatt, D., Han, X., Smith, Y., and Nedergaard, M. (2013). Glutamate-dependent neuroglial calcium signaling differs between young and adult brain. Science *339*, 197–200.

Takano, T., He, W., Han, X., Wang, F., Xu, Q., Wang, X., Oberheim Bush, N.A., Cruz, N., Dienel, G.A., and Nedergaard, M. (2014). Rapid manifestation of reactive astrogliosis in acute hippocampal brain slices. Glia *62*, 78–95.

Treweek, J.B., and Gradinaru, V. (2016). Extracting structural and functional features of widely distributed biological circuits with single cell resolution via tissue clearing and delivery vectors. Curr. Opin. Biotechnol. *40*, 193–207.

von Poser, C., Ichtchenko, K., Shao, X., Rizo, J., and Südhof, T.C. (1997). The evolutionary pressure to inactivate. A subclass of synaptotagmins with an amino acid substitution that abolishes Ca2+ binding. J. Biol. Chem. *272*, 14314–14319.

Zamanian, J.L., Xu, L., Foo, L.C., Nouri, N., Zhou, L., Giffard, R.G., and Barres, B.A. (2012). Genomic analysis of reactive astrogliosis. J. Neurosci. *32*, 6391–6410.

Zhang, Y., and Barres, B.A. (2010). Astrocyte heterogeneity: an underappreciated topic in neurobiology. Curr. Opin. Neurobiol. *20*, 588–594.

Zhang, Y., Chen, K., Sloan, S.A., Bennett, M.L., Scholze, A.R., O'Keeffe, S., Phatnani, H.P., Guarnieri, P., Caneda, C., Ruderisch, N., et al. (2014). An RNA-sequencing transcriptome and splicing database of glia, neurons, and vascular cells of the cerebral cortex. J. Neurosci. *34*, 11929–11947.

STAR★METHODS

KEY RESOURCES TABLE

REAGENT or RESOURCE	SOURCE	IDENTIFIER
Antibodies		
chicken anti-GFP	Abcam	Cat#ab13970; RRID: AB_300798
rabbit anti-GFP	Molecular Probes	Cat#A11122; RRID: AB_221569
mouse anti-NeuN (clone A60)	Millipore	Cat#MAB377; RRID: AB_2298772
mouse anti-mCherry	Saint John's	Cat#STJ97087
rabbit anti-S100β	Abcam	Cat#ab41548; RRID: AB_956280
chicken anti-GFAP	Abcam	Cat#ab4674; RRID: AB_304558
guinea pig anti-GLT1	Millipore	Cat#AB1783; RRID: AB_90949
rabbit anti-KIR4.1	Alomone	Cat#APC-035; RRID: AB_2040120
mouse anti-μ-crystallin	Santa Cruz	Cat#sc-376687; RRID: AB_11150103
rabbit anti-β-actin	Abcam	Cat#ab8227; RRID: AB_2305186
mouse anti-HA.11 antibody (clone 16B12)	Covance	Cat#MMS-101R; RRID: AB_291263
Alexa goat anti-rabbit 488	Molecular Probes	Cat#A11008; RRID: AB_143165
Alexa goat anti-chicken 488	Molecular Probes	Cat#A11039; RRID: AB_142924
streptavidin conjugated Alexa 488	Molecular Probes	Cat#S32354; RRID: AB_2315383
Alexa goat anti-rabbit 546	Molecular Probes	Cat#A11010; RRID: AB_143156
Alexa goat anti-mouse 546	Molecular Probes	Cat#A11003; RRID: AB_141370
streptavidin conjugated Alexa 555	Molecular Probes	Cat#S32355; RRID: AB_2571525
Alexa goat anti-guinea pig 546	Molecular Probes	Cat#A11074; RRID: AB_2534118
Alexa goat anti-rabbit 647	Molecular Probes	Cat#A21245; RRID: AB_2535813
IRDye 800CW anti-rabbit	Li-Cor	Cat#827-08365; RRID: AB_10796098
IRDye 680RD anti-mouse	Li-Cor	Cat#926-68170; RRID: AB_10956589
Bacterial and Virus Strains		
AAV2/5 GfaABC$_1$D-cyto-GCaMP6f	Haustein et al., 2014; UPenn Vector Core	Cat#AV-5-52925
AAV2/5 GfaABC$_1$D-hM3D-mCherry	This paper	N/A
AAV2/5 GfaABC$_1$D-hM4D-mCherry	This paper	N/A
AAV2/5 GfaABC$_1$D-rM3D-mCherry	This paper	N/A
AAV2/5 GfaABC$_1$D-iGluSnFr	Haustein et al., 2014; UPenn Vector Core	Cat#AV-5-PV4618
Chemicals, Peptides, and Recombinant Proteins		
Paraformaldehyde, EM grade	EMS	Cat#19202
Lucifer yellow CH dilithium salt	Sigma-Aldrich	Cat#L0259
Sodium cadodylate	EMS	Cat#12300
Glutaraldehyde	Polysciences	Cat#1909
Biocytin	Tocris	Cat#3349
TTX	Cayman Chemical Company	Cat#14964
Bicuculline	Sigma-Aldrich	Cat#14340
CNQX disodium salt	Abcam	Cat#ab120044
Carbenoxolone	Tocris	Cat#3096
Cyclopiazonic acid (CPA)	Tocris	Cat#1235
Clozapine N-oxide (CNO)	Tocris	Cat#4936
Tamoxifen	Sigma-Aldrich	Cat#T5648
TFB-TBOA	Tocris	Cat#2532

(*Continued on next page*)

Continued

REAGENT or RESOURCE	SOURCE	IDENTIFIER
Phenylephrine	Tocris	Cat#2838
DHPG	Tocris	Cat#0342
A77636	Tocris	Cat#1701
LY354740	Tocris	Cat#3246
Sumanirole	Tocris	Cat#2773
PD128907	Tocris	Cat#1243
R-baclofen	Tocris	Cat#0796
Trypsin	Promega	Cat#V5111
Papain	Worthington	Cat#LS003126
Ovomucoid trypsin inhibitor	Worthington	Cat#LS003086
EBSS	Sigma-Aldrich	Cat#E7510
DNase I	Worthington	Cat#2006
Halt protease inhibitor cocktail	Thermo	Cat#1861278
Critical Commercial Assays		
Ovation PicoSL WTA System V2	Nugen	Cat#3312
Nugen Ovation RNA-seq System V2	Nugen	Cat#7102
QIAquick PCR Purification Kit	QIAGEN	Cat#28104
QIAGEN Rneasy Plus Micro Kit	QIAGEN	Cat#74034
Illumina MouseRef-8 v2.0 expression BeadChip	Illumina (no longer available)	Cat#BD-202-0202
Pierce BCA protein assay kit	Thermo Scientific	Cat#23225
Deposited Data		
Raw and normalized RNA-seq data	This paper	GEO: GSE94010
Proteomic data	This paper	PRIDE: PXD005852
Experimental Models: Organisms/Strains		
Mouse: *Aldh1l1*-eGFP	MMRRC	Stock#011015-UCD; RRID: MMRRC_011015-UCD
Mouse: Swiss-Webster outbred mice	Taconic	Stock#Tac:SW
Mouse: B6N.129-*Rpl22*$^{tm1.1Psam}$/J	Jackson Laboratory	Stock#011029; RRID: IMSR_JAX:011029
Mouse: *Aldh1l1*-cre/ERT2	Jackson Laboratory	Stock#029655; RRID: IMSR_JAX:029655
Mouse: C57BL/6NTac inbred mice	Taconic	Stock#B6
Oligonucleotides		
Primers for *Crym* qPCR: 5′ TGCAAGGAGATGTTCGGGTC 3′; 5′ CATCCAGTTCTCGCCAGTCA 3′	This paper	N/A
Primers for *Gfap* qPCR: 5′ AGAACAACCTGGCTGCGTAT 3′; 5′ CTTGGCCACATCCATCTCCA 3′	This paper	N/A
Primers for *Arbp* qPCR: 5′ TCCAGGCTTTGGGCATCA 3′; 5′ AGTCTTTATCAGCTGCACATCAC 3′	Jiang et al., 2016	N/A
Software and Algorithms		
OriginPro 8.5/9/2015	Origin Lab	N/A
GraphPad Instat 3	GraphPad Software	N/A
pCLAMP10	Molecular Devices	N/A
ClampFit 10.5	Molecular Devices	N/A
Fluoview FV3000	Olympus	N/A
ImageJ v1.30	ImageJ	N/A
MiniAnalysis 6.0.3	Synaptosoft	http://www.synaptosoft.com/MiniAnalysis/
GECIquant	Srinivasan et al., 2015	N/A
Imaris version 7.6.5	Bitplane	N/A
Reconstruct software version 1.1	Fiala, 2005	https://synapseweb.clm.utexas.edu/software-0

(*Continued on next page*)

Continued

REAGENT or RESOURCE	SOURCE	IDENTIFIER
R v3.3.2	RCoreTeam, 2016	N/A
Bioconductor	Law et al., 2014	http://www.bioconductor.org
Htseq-count	Anders et al., 2015	N/A
Gene Set Enrichment Analysis	Broad Institute	http://software.broadinstitute.org/gsea/
Illumina Bcl2fastq2 v 2.17	Illumina	N/A
Illumina BeadStudio	Illumina	N/A
Sequest	Thermo	N/A
Thermo Proteome discoverer 1.4	Thermo	N/A
Image Studio Lite software	Li-Cor	N/A
Other		
Resource website for RNA-seq and Proteomics	This paper	http://astrocyternaseq.org

CONTACT FOR REAGENT AND RESOURCE SHARING

Further information and requests for resources and reagents should be directed to and will be fulfilled by the Lead Contact, Baljit S. Khakh (bkhakh@mednet.ucla.edu).

EXPERIMENTAL MODEL AND SUBJECT DETAILS

All animal experiments were conducted in accordance with the National Institute of Health Guide for the Care and Use of Laboratory Animals and were approved by the Chancellor's Animal Research Committee at the University of California, Los Angeles. All mice were housed with food and water available ad libitum in a 12 hr light/dark environment. All animals were healthy with no obvious behavioral phenotype, were not involved in previous studies, and were sacrificed during the light cycle. Data for experiments were collected from adult mice (8-11 weeks old for most experiments, 3-4 weeks old for electrophysiology, and 4-5 weeks old for proteomics and microarrays). Both male and female mice were used.

Mouse models

Aldh1l1-eGFP (MMRRC #3843271) on a Swiss-Webster background were acquired from MMRRC and maintained by breeding with Swiss-Webster mice (from Taconic). Hemizygous transgenic mice and wild-type littermates were used for experiments. B6N.129-*Rpl22*$^{tm1.1Psam}$/J (JAX# 011029) were acquired from the Jackson Laboratory and bred with *Aldh1l1*-cre/ERT2 mice (Srinivasan et al., 2016) (N3 backcrossed to C57BL/6N from Taconic) from an in-house colony; hemizygous transgenic heterozygous knock-in mice were used for RNA-seq experiments.

METHOD DETAILS

Experimental design

Data from every experiment represent a minimum of three animals using a balanced number of male and female mice. Sample sizes were not calculated a priori. For AAV injections, mice were randomly assigned to striatal or hippocampal group. In calcium imaging experiments where agonists were applied sequentially (endogenous G protein coupled receptor agonists), the sequence of drug application was randomized and each slice received at most three different agonists. For RNA-seq, the dissection and homogenization order of brain regions alternated with every animal. For FACS, the sorting order of striatum and hippocampal cells alternated with every run.

Stereotaxic microinjections of adeno-associated viruses

Stereotaxic injections into the mouse hippocampus and striatum were performed as previously described (Jiang et al., 2014, 2016; Shigetomi et al., 2013). Mice (P42-49) were used in all surgeries in accordance with institutional guidelines. All surgical procedures were conducted under general anesthesia using continuous isoflurane (induction at 5%, maintenance at 1%–2.5% vol/vol). Depth of anesthesia was monitored continuously and adjusted when necessary. Following induction of anesthesia, the mice were fitted into a stereotaxic frame with their heads secured by blunt ear bars and their noses placed into an anesthesia and ventilation system (David Kopf Instruments). Mice were administered 0.1 mg/kg of buprenorphine (Buprenex, 0.1 mg/ml) subcutaneously before surgery. The surgical incision site was then cleaned three times with 10% povidone iodine and 70% ethanol (vol/vol). Skin incisions were made, followed by craniotomies of 2–3 mm in diameter above the left frontal or parietal cortex using a small steel burr (Fine Science Tools) powered by a high-speed drill (K.1070, Foredom). Saline (0.9%) was applied onto the skull to reduce heating caused by drilling.

Unilateral viral injections were carried out by using a stereotaxic apparatus (David Kopf Instruments) to guide the placement of beveled glass pipettes (1B100-4, World Precision Instruments). For the left hippocampus: the coordinates were 2 mm posterior to bregma, 1.5 mm lateral to midline, and 1.6 mm from the pial surface. For the left striatum: the coordinates were 0.8 mm anterior to bregma, 2 mm lateral to midline, and 2.4 mm from the pial surface. Adeno-associated viruses (AAVs) were injected by using a syringe pump (Pump11 PicoPlus Elite, Harvard Apparatus). Glass pipettes were left in place for at least 10 min prior to slow withdraw. Surgical wounds were closed with external 5-0 nylon sutures. Following surgery, animals were allowed to recover overnight in cages placed partially on a low-voltage heating pad. Buprenorphine was administered two times per day for up to 2 days after surgery. In addition, trimethoprim sulfamethoxazole was provided in food to the mice for 1 week. Virus injected mice were euthanized two to three weeks post surgery for live slice imaging or perfused for immunohistochemistry. Viruses used were: 1.3 μL of AAV2/5 GfaABC$_1$D-cyto-GCaMP6f virus (3 × 10^{10} genome copies); 1.3 ul of AAV2/5 GfaABC$_1$D-HM3D-mCherry, HM4D-mCherry, or RM3D-mCherry virus (~10^{10} genome copies); 1.3 μL of AAV2/5 GfaABC$_1$D-iGluSnFr virus (6 × 10^9 genome copies). Two viruses were co-injected for DREADD calcium and glutamate imaging; the injections in those cases were as follows: 1.3 ul of AAV2/5 GfaABC$_1$D-cyto-GCaMP6f virus with AAV2/5 GfaABC$_1$D-HM3D-mCherry, HM4D-mCherry, or RM3D-mCherry virus (~10^{10} genome copies each); 1.3 μL of AAV2/5 GfABC$_1$D-iGluSnFr with AAV2/5 GfABCD$_1$-HM3D-mCherry virus (4 × 10^9 genome copies each).

In vivo activation of HM4D

Two weeks after unilateral injection of hM4D-mCherry AAV into the striatum and hippocampus of *Aldh1l1*-eGFP mice, CNO was administered to animals with intraperitoneal injection (1 mg/kg; dissolved in saline). One hour after CNO administration, animals were sacrificed and used for immunohistochemistry.

Immunohistochemistry (IHC)

For transcardial perfusion, mice were euthanized with pentobarbitol (i.p.) and perfused with 10% buffered formalin (Fisher #SF100-20). Briefly, once all reflexes subsided, the abdominal cavity was opened and heparin (50 units) was injected into the heart to prevent blood clotting. The animal was perfused with 20 mL ice cold 0.1 M phosphate buffered saline (PBS) followed by 60 mL 10% buffered formalin. After gentle removal from the skull, the brain was postfixed in 10% buffered formalin overnight at 4°C. The tissue was cryoprotected in 30% sucrose PBS solution the following day for at least 48 hr at 4°C until use. 40 μm coronal sections were prepared using a cryostat microtome (Leica) and processed for immunohistochemistry. For staining of acute slices, 300 μm slices were placed into 10% buffered formalin overnight at 4°C and processed as follows for IHC. Sections were washed 3 times in 0.1 M PBS for 10 min each, and then incubated in a blocking solution containing 10% NGS in 0.1 M PBS with 0.5% Triton X-100 for 1 hr at room temperature with agitation. Sections were then incubated with agitation in primary antibodies diluted in 0.1 M PBS with 0.5% Triton X-100 overnight at 4°C. The following primary antibodies were used: chicken anti-GFP (1:1000; Abcam ab13970), rabbit anti-GFP (1:1000; Molecular Probes A11122), mouse anti-NeuN (1:1000; Millipore MAB377), mouse anti-mCherry (1:1000; Saint John's STJ97087), rabbit anti-S100β (1:1000; Abcam ab41548), chicken anti-GFAP (1:1000; Abcam ab4674), Guinea pig anti-GLT1 (1:2500; Millipore AB1783), rabbit anti-KIR4.1 (1:1500; Alomone APC-035), and mouse anti-μ-crystallin (1:250; Santa Cruz sc-376687). The next day the sections were washed 3 times in 0.1 M PBS for 10 min each before incubation at room temperature for 2 hr with secondary antibodies diluted in 0.1 M PBS. The following Alexa conjugated (Molecular Probes) secondary antibodies were used: goat anti-chicken 488 (1:1000), goat anti-rabbit 488 (1:1000), streptavidin conjugated Alexa 488 (1:250), streptavidin conjugated Alexa 555 (1:250), goat anti-rabbit 546 (1:1000), goat anti-mouse 546 (1:500), goat anti-guinea pig 546 (1:1000), and goat anti-rabbit 647 (1:1000). The sections were rinsed 3 times in 0.1 M PBS for 10 min each before being mounted on microscope slides in fluoromount-G. Fluorescent images were taken using UplanSApo 20X 0.85 NA and UplanFL 40X 1.30 NA oil immersion objective lens on a confocal laser-scanning microscope (Fluoview 1000; Olympus). We used the 488 nm line of an Argon laser to excite Alexa488, with the intensity adjusted to 4% of the maximum output, which was 10 mW. The emitted light pathway consisted of an emission high pass filter (505-525 nm) before the photomultiplier tube. Alexa 546 was excited by the 543 nm laser line of the HeNeG laser at 20%–25% of the maximum output (1 mW). The emitted light pathway consisted of a dichroic mirror (SDM560) and a 560–600 nm emission filter. Laser settings were kept the same within each experiment. Images represent maximum intensity projections of optical sections with a step size of 1.0 μm.

Images were processed with ImageJ. Cell counting was done on maximum intensity projections using the Cell Counter plugin; only cells with soma completely within the region of interest (ROI) were counted. For signal area and intensity measurements, ROIs were created using the same intensity threshold in experimental and control images.

Acute brain slice preparation for imaging and electrophysiology

Slice procedures have been described previously (Jiang et al., 2016; Shigetomi et al., 2013). Coronal striatal or hippocampal slices were prepared from 8-11 week old Swiss-Webster mice with AAV injection for imaging or from 3-4 week old Aldh1l1-eGFP and WT littermates for electrophysiology. Briefly, animals were deeply anesthetized with isoflurane and decapitated. The brains were placed and sliced in ice-cold modified artificial CSF (aCSF) containing the following (in mM): 194 sucrose, 30 NaCl, 4.5 KCl, 1 $MgCl_2$, 26 $NaHCO_3$, 1.2 NaH_2PO_4, and 10 D-glucose, saturated with 95% O_2 and 5% CO_2. A vibratome (DSK-Zero1) was used to cut 300 μm brain sections. The slices were allowed to equilibrate for 30 min at 32-34°C in normal aCSF containing (in mM); 124 NaCl, 4.5 KCl, 2 $CaCl_2$, 1 $MgCl_2$, 26 $NaHCO_3$, 1.2 NaH_2PO_4, and 10 D-glucose continuously bubbled with 95% O_2 and 5% CO_2. Slices

were then stored at 21–23°C in the same buffer. All experiments were performed within 4-6 hr of slicing. We are aware that neurons and astrocytes can change in brain slices under some circumstances (Fiala et al., 2003; Takano et al., 2014), but our procedures were standardized, all relevant experiments were performed within 4-6 hr of slicing and the conditions were identical for hippocampus and striatum. Also, our procedures are identical to those routinely used for several decades to study both astrocytes and neurons. Moreover, our core conclusions related to astrocyte similarities and differences between hippocampus and striatum were reproduced using parallel methods, which did not require brain slices. Finally, we have previously discussed the similarity between astrocyte calcium signaling in slices and in vivo under our experimental conditions (Khakh and Sofroniew, 2015; Shigetomi et al., 2016). Hence, we do not think slice procedures contribute markedly to our conclusions, but nonetheless our findings should be interpreted with these considerations in mind.

Electrophysiological recording and assessment of dye coupling in brain slices

Slices were placed in the recording chamber and continuously perfused with 95% O_2 and 5% CO_2 bubbled normal aCSF. Cells were visualized with infrared optics on an upright microscope (BX51WI, Olympus). pCLAMP10 software and a Multi-Clamp 700B amplifier was used for electrophysiology (Molecular Devices). For recording from striatal medium spiny neurons and hippocampal CA1 pyramidal neurons, currents were measured in whole-cell mode using pipettes with a typical resistance of 5–6 MΩ when filled a K^+ internal solution consisting of the following (in mM): 135 potassium gluconate, 5 KCl, 0.5 $CaCl_2$, 5 HEPES, 5 EGTA, 2 Mg-ATP and 0.3 Na-GTP, pH 7.3 adjusted with KOH. In some cases, 2 mg/ml biocytin was added to the intracellular solution to subsequently visualize patched neuron. Neurons were voltage-clamped at −70 mV unless otherwise stated. Extrasynaptic NMDA-mediated slow inward currents were recorded in low-Mg^{2+} buffer (0.1 mM) in the presence of bicuculline (10 μM), TTX (250 nM), and 6-cyano-2,3-dihydroxy-7-nitroquinoxaline (CNQX; 10 μM). ClampFit 10.5 software was used to analyze traces from neuronal recordings.

For recording from astrocytes and dye coupling experiments, currents were measured in whole-cell mode using pipettes with a typical resistance of 5.5 MΩ when filled with internal solution containing the following (in mM): 130 K-gluconate, 2 $MgCl_2$, 10 HEPES, 5 EGTA, 2 Na-ATP, 0.5 $CaCl_2$, with pH set to 7.3. 2 mg/ml biocytin was added to the intracellular solution to examine gap junction coupling. Astrocytes were held in whole-cell mode for 30 min to allow biocytin to diffuse from the patched cell to other cells connected by gap junctions. In some cases CBX (100 μM) was added to the recording solution to block gap junctions. Brain slices were then rescued from the recording chamber for IHC.

Intracellular Ca^{2+} and cell surface glutamate imaging

Slice preparation was performed as above. Cells for all the experiments were imaged using a confocal microscope (Fluoview 1000; Olympus) with a 40X water-immersion objective lens with a numerical aperture (NA) of 0.8 and at a digital zoom of two to three. For EFS-evoked signals, zoom of 1.5 was used. We used the 488 nm line of an Argon laser, with the intensity adjusted to 10%–14% of the maximum output of 10 mW. The emitted light pathway consisted of an emission high pass filter (505-525 nm) before the photomultiplier tube. For animals that received DREADD viruses, the 543 nm line of the HeNeG laser with intensity adjusted to 20% of the maximum output of 1 mW was used. Astrocytes were typically ~25 μm below the slice surface and scanned at 1 frame per second for imaging sessions (CPA Ca^{2+}-free experiments were scanned at 1 frame per 5 s). For EFS-evoked signals, stimulus electrode was placed at the stratum radiatum of CA1 and corpus callosum for hippocampal and striatal astrocytes, respectively. Ca^{2+} and glutamate imaging were performed at 150-300 μm away from the electrode. For pharmacological activation of DREADDs and endogenous GPCRs, agonists (see Key Resources Table) were dissolved in either water or DMSO for minimum 1000X stock solution. Stock solutions were diluted in aCSF immediately prior acute bath application.

Calcium imaging analysis

Analyses of time-lapse image series were performed using ImageJ v1.30 (NIH). XY drift was corrected using ImageJ; cells with Z-drift were excluded from analyses. The data were analyzed essentially as previously reported (Haustein et al., 2014; Srinivasan et al., 2015, 2016). Using ImageJ v1.30 (NIH) and GECIquant (Srinivasan et al., 2015), time traces of fluorescence intensity were extracted from the ROIs and converted to dF/F values. For analyzing spontaneous Ca^{2+} signaling, regions of interest (ROIs) were defined in normal aCSF (control) and the same ROIs were used to analyze the effect of TTX. Separately, to analyze the effect of removal of extracellular Ca^{2+}, ROIs were defined in TTX and the same ROIs were used to analyze the effect of TTX Ca^{2+}-free buffer. To compare between striatal and hippocampal astrocytes, ROIs were generated for control, TTX, and TTX Ca^{2+}-free conditions individually. Using MiniAnalysis 6.0.07 (Synaptosoft), spontaneous events were manually marked. Event amplitudes, half width and event frequency per ROI per min was measured. Events were identified based on amplitudes that were at least 2-fold above the baseline noise of the dF/F trace.

For all other calcium imaging experiments, extracted calcium signals were analyzed using OriginPro 8.5 (OriginLab). For EFS-evoked signals, whole astrocyte territories were selected as ROIs. For Ca^{2+} homeostasis experiments (Figure S2D), only the somatic fluorescence intensity was extracted. For DREADD experiments, time traces of fluorescence intensity were extracted from somata and processes. Using OriginPro, the integrated area-under-the-curve (AUC) of dF/F traces was analyzed. AUC per minute in baseline condition versus the first two minutes of CNO application was used for paired comparisons per cell. Two minutes of CNO was chosen to capture the peak response that was clearly visible from the traces. For endogenous GPCR experiments, somata AUC per minute during baseline condition versus during the two minutes after agonist hits the slice chamber were compared. As elevation of Ca^{2+} in processes lasted a shorter amount of time, processes' AUC per minute during baseline condition versus during the one minute after

agonist hits the slice chamber was compared. Fold change was used to compare agonist responses between regions, and was defined as the ratio of agonist versus baseline AUC per minute.

Glutamate imaging analysis

Glutamate signals were extracted using GECIquant soma function thresholded to encompass the whole astrocyte territory and then analyzed in OriginPro 8.5. Peaks in dF/F traces with twice the change in dF/F as baseline noise were deemed iGluSnFR flashes.

Brain tissue clearing

Sca*l*eS tissue clearing was performed on *Aldh1l1*-eGFP mice as previously described (Hama et al., 2015) to allow for deeper imaging of endogenous fluorescence while preserving the three-dimensional architecture. P70-80 mice were given 100 units of heparin with intraperitoneal injection to prevent blood clotting and then euthanized with barbiturate overdose prior to transcardial perfusion with 50 mL of ice-cold 0.1 M PBS, followed by 50 mL of ice-cold 4% paraformaldehyde (EMS #19202). Brains were gently removed from the skull and post-fixed overnight at 4°C. One millimeter-thick coronal sections of striatum and hippocampus were cut using Pelco Vibrotome 3000. Brain sections were then cleared using the Sca*l*eSQ(5) protocol. Briefly, sections were incubated in Sca*l*eSQ(5) (22.5% D-(-)-sorbitol [w/v], 9.1 M urea and 5% Triton X-100 [w/v] in distilled water; pH 8.2) for 2 hr at 37°C under gentle agitation. Samples were then mounted overnight in Sca*l*eS4(0) (40% D-(-)-sorbitol [w/v], 10% glycerol [w/v], 4 M urea and 15% dimethylsulfoxide [v/v] in distilled water; pH 8.1; refractive index 1.437). Cleared sections were imaged using a Zeiss LSM 780 confocal microscope, and semi-automated cell counting of astrocytes and was performed using Imaris version 7.6.5 (Bitplane). The volumes of the brain regions counted were measured using Imaris surface function.

Astrocyte intracellular Lucifer yellow iontophoresis

This method for filling cells in fixed tissue was modified from published methods (Bushong et al., 2002). Swiss-Webster wild-type mice (P44-58) were euthanized with barbiturate overdose and transcardially perfused with 10 mL of 35°C Ringer's Solution with 0.02% lidocaine followed by 4% paraformaldehyde. Ringer's Solution contains the following (in mM): 135 NaCl, 14.7 $NaHCO_3$, 5 KCl, 1.25 Na_2HPO_4, 2 $CaCl_2$, 1 $MgCl_2$, and 11 D-glucose, bubbled with 95% O_2 and 5% CO_2. Brains were lightly post-fixed at room temperature for 1.5 hr and then washed three times in ice cold 0.1 M PBS for 10 min. 100 μm coronal sections were cut using Pelco Vibrotome 3000 and then placed in ice-cold PBS for the duration of the experiment. 10 mg Lucifer yellow CH di-Lithium salt (Sigma) was dissolved in 1 mL 5 mM KCl solution and filtered prior to use. Sharp (~200 MOhm) glass electrodes were pulled from Borosilicate glass capillary with filament (O.D. 1.0 mm, I.D. 0.58 mm). Electrodes were gravity filled. Sections were transferred to a solution of room temperature PBS for filling. Astrocytes were identified using IR-DIC and then impaled with the sharp electrode. Lucifer yellow was ejected into the cell by passing current (~2 μA) for ~20 s: three times with 15-20 s pauses in between. Sections were post-fixed completely with 4% PFA at 4°C prior to mounting on glass slides. In some cases, sections were processed for IHC co-staining with NeuN. Cells were imaged using a Zeiss LSM 780 confocal microscope, with UplanFL 40X 1.30 NA oil immersion objective lens with 0.25 um z-steps and 2.5-3.5x zoom.

Quantitative volumes were generated using Imaris' surface function. The astrocyte cell volume was segmented by raw intensity to create faithful representation of the extremely bright soma and primary branches, as well as the finer astrocyte processes. For the soma, surface smoothing was set at the *x-y* plane resolution limit (0.25 μm) and minimum seed object diameter was set to 3.0 μm. The reconstruction of soma was used to mask the raw confocal volume and the masked intensity was used to reconstruct the major processes. For major branches, surface smoothing and minimum seed object diameter were set to Z plane step size (0.25 μm). The reconstruction of major branches was used to further mask the confocal signal, leaving the fluorescent intensity from only the fine processes. For the fine astrocyte processes, surface smoothing was set at the *x-y* plane resolution limit (0.18 μm) and minimum seed object diameter was set to Z plane step size (0.25 μm). Summation of the soma, branches, and processes reconstruction volumes provided the astrocyte cell volume. The astrocyte territory volume was measured from a low-intensity threshold reconstruction (surface smoothing 0.75 μm) encompassing the cell volume and the space between its processes. NeuN co-staining was reconstructed as low threshold surfaces, and the number of neuronal cell bodies that intersect with the astrocyte territory is counted. The number of primary branches was counted visually.

Electron Microscopy

Swiss-Webster wild-type mice (P59-P64; 2 males, 1 female) were euthanized with barbiturate overdose and transcardially perfused with the following solution at 6 ml/min for 10 min: 4% paraformaldehylde (EMS #19202) and 2.5% glutaraldehyde (Polysciences #1909) in a 0.1 M sodium cadodylate (EMS #12300) buffer (pH 7.2). Brains were sliced into 1 mm coronal sections and then further dissected to the regions of interest: dorsal lateral striatum and hippocampus CA1. Tissues were post-fixed in perfusion solution for 48 hr at 4°C. Fixed tissues were prestained with 0.1% tannic acid, and then stained with osmium-ferrocyanide, followed by tetracarbohydrazide treatment, and then further stained with 2% aqueous osmium tetroxide. Samples were then incubated overnight in saturated aqueous uranyl acetate, followed by Walton's lead aspartate stain. Next, samples were dehydrated through a series of alcohol, followed by propylene oxide, a 50/50 propylene oxide and resin mixture, before being embedded in Epon 812-substitute resin. The resin blocks were then trimmed and mounted on an aluminum pin, coated with colloidal silver paste around the block edges, and then examined in a Zeiss Sigma VP system equipped with a Gatan 3View in-chamber ultramicrotome stage with low-kV backscattered electron detectors optimized for 3View systems. Samples were routinely imaged at 2.25kV, at 6.8nm/pixel resolution, with field sizes

between 40-50 um in *x-y* and slice thickness of 80 nm. The acquisition of the EM data was performed by Renovo Neural (Cleveland, Ohio). Image series were registered and then analyzed using Reconstruct software version 1.1 ((Fiala); https://synapseweb.clm.utexas.edu/software-0).

Striatal medium spiny neuron (MSN) spines and hippocampal CA1 pyramidal neuron spines in the stratum radiatum were traced. Striatal MSNs have aspiny primary dendrites that become spiny upon branching. Only dendrites whose aspiny primary and spiny secondary or tertiary portions were found in the image series were analyzed. Hippocampal CA1 pyramidal neurons have apical dendrites that run largely orthogonal to the pyramidal cell layer. A low magnification blockface image was used to orient hippocampal image series. At least three dendrites were analyzed from one or two serial section series per region per mouse. All spines on selected dendrites were traced along with their corresponding pre-synaptic axon bouton and nearby astrocyte processes. Astrocyte processes were identified by their persistent irregular shape through multiple sections and by the presence of glycogen granules. The postsynaptic density (PSD) of each spine was traced and the estimated center of the PSD marked. Spine types were defined as previously described (Harris et al., 1992) into mushroom, thin, and other (stubby and branched) using 3D rendering of the traces. Mushroom spines have spine head diameter much greater than neck diameter; thin spines have spine head diameter similar to neck diameter and spine length much greater than neck diameter. Stubby spines have spine length similar to neck diameter; branched spines have more than one spine head. The shortest distance (straight line) between the center of the PSD and nearby astrocyte processes was measured for each traced synapse using the ''Distance'' function in Reconstruct software.

RNA-seq determination of striatal and hippocampal astrocyte transcriptomes and analyses

Adult (P63) *Aldh1l1*-cre/ERT2 x Ribotag mice (2 males and 2 females) were used to purify RNA from astrocytes as previously described (Srinivasan et al., 2016). Tamoxifen (Sigma, 20 mg/ml) was administered intraperitoneally for five consecutive days at 75 mg/kg. Experiments were performed two weeks after the last tamoxifen injection. RNA was collected from hippocampi and striata of *Aldh1l1*-cre/ERT2 x RiboTag mice based on a published protocol (Sanz et al., 2009). Briefly, freshly dissected tissues were collected from four animals and individually homogenized. RNA was extracted from 20% of cleared lysate as input. The remaining lysate was incubated with mouse anti-HA antibody (1:250; Covance #MMS-101R) with rocking for 4 hr at 4°C followed by addition of magnetic beads (Invitrogen Dynabeads #110.04D) and overnight incubation with rocking at 4°C. The beads were washed three times in high salt solution. RNA was purified from the IP and corresponding input samples (QIAGEN Rneasy Plus Micro #74034). RNA concentration and quality were assessed with nanodrop and Agilent 2100 Bioanalyzer. RNA samples with RNA integrity number (RIN) greater than eight (mean RIN 8.6; range 8.1-9.3) were used for multiplexed library prep with Nugen Ovation RNA-seq System V2. Sequencing was performed on Illumina NextSeq 500 for 2x75. Data quality check was done on Illumina SAV. Demultiplexing was performed with Illumina Bcl2fastq2 v 2.17 program. Reads were aligned to the latest mouse mm10 reference genome using the STAR spliced read aligner (~88% reads mapped uniquely). Fragment counts were derived using HTS-seq program (Anders et al., 2015). Principal component analysis was performed using R v3.3.2 (RCoreTeam, 2016) using the 2000 most variable genes across all samples. Analysis of differential expression was performed using the Bioconductor LIMMA package (Law et al., 2014). The list of genes sequenced in striatal and/or hippocampal IP samples were ranked by LimmaVoom log ratio with no false discovery rate (FDR) threshold and used for Gene Set Enrichment Analysis (GSEA) (http://software.broadinstitute.org/gsea/). Differentially expressed (DE) genes were identified using Bioconductor packages (http://www.bioconductor.org) and Limma-Voom with adjustment for difference between animals using FDR threshold < 0.05 for all comparisons.

RNA and protein extraction from astrocytes isolated by FACS

Aldh1l1-eGFP mice were used to purify astrocytes by fluorescence-activated cell sorting (FACS). Whole hippocampi or striata from heterozygous P30 mice were dissociated following published guidelines (Foo, 2013) with slight modifications. Briefly, the hippocampi and striata from four mice (two male and two females) were dissected and digested together for 45 min at 36°C in a 35 mm Petri dish with 2.5 mL of papain solution (1x EBSS, 0.46% D-glucose, 26 mM $NaHCO_3$, 50 mM EDTA, 75 U/ml DNase1, 200 units of papain for hippocampal and 300 units of papain for striatal tissue, and 2 mM L-cysteine) while bubbling with 5% CO_2 and 95% O_2. After digestion, the tissue was washed four times with ovomucoid solution (1x EBSS, 0.46% D-glucose, 26 mM $NaHCO_3$, 1 mg/ml ovomucoid, 1 mg/ml BSA, and 60 U/ml DNase1) and mechanically dissociated with two fire-polished borosilicate glass pipettes with different bore sizes. A bottom layer of concentrated ovomucoid solution (1x EBSS, 0.46% D-glucose, 26 mM $NaHCO_3$, 5. mg/ml ovomucoid, 5.5 mg/ml BSA, and 25 U/ml DNase1) was added to the cell suspension. The tubes were centrifuged at room temperature at 300 *g* for 10 min and the resultant pellet was re-suspended in D-PBS with 0.02% BSA and 13 U/ml of DNase1, and filtered with a 20 μm mesh. FACS was performed in a FACSAria II (BD Bioscience) with a 70 μm nozzle using standard methods at the University of California, Los Angeles (UCLA) Cell Sorting Core. For RNA extraction, sorted cells were collected in D-PBS with 0.1% BSA, and centrifuged for 10 min at 4°C and 2000 g. The RNA was extracted from the pelleted cells using RNeasy Plus Micro Kit (QIAGEN). For protein extraction, cells were collected in D-PBS and, right after FACS, cells were incubated with lysis buffer (150 mM NaCl, 1% Triton X-100, 12 mM Na^+-Deoxycholate, 3.5 mM sodium dodecyl sulfate, 50 mM Tris pH8, 1:100 Halt Protease Inhibitor cocktail (Thermo Scientific)) at 4°C for 40 min. The extracted protein was subsequently precipitated with trifluoroacetic acid and acetone. Protein pellet was dried and resuspended in a proteomics compatible buffer (0.5% Na-Deoxycholate, 12 mM N-Lauroylsarcosine sodium salt, 50 mM triethylammonium bicarbonate), boiled at 95°C for 10 min and stored at −80°C.

Microarrays of FACS astrocytes

RNA was extracted from eGFP-negative, eGFP-positive and unsorted cells, i.e., cells that went through FACS but were not separated based on the GFP fluorescence. eGFP-negative and eGFP-positive cells obtained from three separate sorts (2 males and 2 females each), and unsorted cells from two, were used for microarray hybridization. RNA from both striatum and hippocampus were extracted from each mouse. RNA quantity was assessed with Nanodrop (Thermo Fisher Scientific), and quality with a bioanalyzer (Agilent Technologies). Samples were processed by the UCLA Neuroscience Genomics Core (UNGC). 3 ng of RNA per sample, with RIN > 7, were amplified using Ovation PicoSL WTA System v2 (Nugen) and 750 ng of biotin-cDNA was used to hybridize with Illumina MouseRef-8 v2.0 expression BeadChip (Illumina). Slides were scanned using BeadStation and signal extracted using Illumina BeadStudio software (Illumina). Raw data was further analyzed using Bioconductor packages (http://www.bioconductor.org). Quality assessment was performed by inter-array Pearson correlation, and clustering based on top variant genes was used to assess overall data coherence. Contrast analysis of differential expression was performed using the Bioconductor LIMMA package. After linear model fitting, a Bayesian estimate of differential expression was calculated. Differences in expression were considered statistically significant at a FDR < 0.05. Principal component analysis was performed using R v3.3.2 (RCoreTeam, 2016) using the 1000 most variable transcripts across all samples.

Mass spectrometry based proteomics

To be able to quantitatively compare the protein expression in striatal and hippocampal astrocytes, we labeled the tryptic peptides produced from proteins originating in each brain region with two isotopically different dimethyl tags, mixed the samples and ran them together in the same LC-MS/MS session. A total of four LC-MS/MS experiments were performed with different protein samples. For one LC-MS/MS experiment, protein from hippocampal or striatal eGFP-positive cells from three cell sorting sessions (12 mice total, 6 females and 6 males; both hippocampal and striatal proteins were obtained from each mouse) were combined and quantified using Pierce BCA protein assay kit (Thermo Scientific) and Nanodrop 2000 (Thermo Scientific). The 11-14 μg of protein obtained per sample was reduced with 5 mM tris(2-carboxyethyl) phosphine (TCEP) for 30 min at RT, and alkylated with 10 mM iodoacetamide (IAA) for 30 min at RT in the dark. Samples were diluted 1:5 (vol/vol) with 50 mM triethylammonium bicarbonate, and 0.1 μg of trypsin/μg of protein was added to each sample and incubated at 37°C. After 4 hr of incubation, same amount of trypsin was added again and incubated at 37°C overnight. The following day, detergent was precipitated out of solution with 0.5% trifluoroacetic acid (final concentration), phase transferred in 1:1 (vol/vol) ethyl acetate, and centrifuged at 16,000 × g. The organic phase was aspirated and the peptides were lyophilized.

Next, stable-isotopic dimethyl labeling was performed. "Light" (+28.0313 Da) or "intermediate" (+32.0564 Da) labels, that are added to the N-terminus and the ε-amino group of lysine residues via reductive amination, were used to tag either striatal or hippocampal samples. The label-brain region combination was shuffled between different LC-MS/MS experiments. Briefly, for light label 0.16% CH_2O and 24 mM $NaBH_3CN$, or 0.16% CD_2O and 24 mM $NaBH_3CN$ for intermediate label, were mixed with the sample at RT for one hour. Reaction was quenched with 0.15% ammonia hydroxide acidified with 0.32% of formic acid, and vacuum dried. Labeled peptides were combined 1:1 (Str:Hip) and fractionated into 10 fractions by strong cationic exchange using Empore cation extraction disks (Empore 2251). Each fraction was desalted with a C18 column and loaded into the HPLC-MS/MS. The fractionated samples were analyzed with an Eskigent 2D nanoLC attached to a Thermo Orbitrap LTQ XL (Thermo Scientific). Peptides were injected onto a laser-pulled nanobore 20 cm x 75 μm C18 column (Acutech Scientific) in buffer A (0.1% formic acid) and resolved using a 2 hr gradient: from 0%–9% buffer B (80% acetonitrile, 20% H_2O with 0.1% formic acid) in 5 min, from 9% to 27% in 90 min, from 27% to 33% in 5 min and from 33% to 50% in 10 min. The Orbitrap XL was operated in data-dependent mode with 60,000 resolution and target autogain control at 5e6 for parent scan. The top 12 ions above a charge of +1 were subjected to collision-induced dissociation set to a value of 35 with target autogain control of 5,000. Dynamic exclusion was set to 30 s.

Mass spectrometry data analysis

Raw data were processed and quantified using Sequest and Thermo Proteome Discoverer (v1.4). The 10 fractions were analyzed together and the Uniprot mouse database was searched with variable modifications of methionine oxidation, fixed modification of cysteine carbamidomethylation, N terminus dimethyl (+28.0313 Da or +32.0564 Da) and lysine dimethyl (+28.0313 Da or +32.0564 Da). Two missed cleavages by trypsin, and 10 ppm and 0.6 Da mass error were allowed on the full MS and tandem MS (MS/MS), respectively. Peptides and proteins were filtered using Percolator with a 1% false discovery rate and maximum delta Cn of 0.05 (low-stringency in the figures and tables). High-stringency protein lists were obtained applying peptide filters (charge state 2-4; score 2.2 for charge state 2, 3.75 for charge state 3, and 5.0 for charge state 4; peptide confidence of FDR < 1%) and protein filters (2 unique peptides per protein required; Sequest score threshold of 10). Ratios between light and intermediate dimethyl labels were calculated per protein and normalized to the ratio of the total protein median. The average area of the three unique peptides with the largest peak area was considered as measurement of abundance of each protein per region. Abundance values were used to perform paired t test to define striatum or hippocampus enriched proteins. At $p < 0.05$ differences were considered significant. In these analyses we assume the two populations contained normally distributed data. Gene ontology analyses were performed using Enrichr (Kuleshov et al., 2016).

qPCR experiments

Amplified cDNA from RNA samples (Ribotag IP and FACS) was generated using Ovation PicoSL WTA System V2 (Nugen). The cDNA was then purified with a QIAquick PCR Purification Kit (QIAGEN) and quantified with a Nanodrop 2000. qPCR was performed in a LightCycler 96 Real-Time PCR System (Roche). Ten nanograms of each sample was loaded per well and gene specific amplification was performed using primers listed in Key Resources Table. Expression levels were calculated based on Ct values of the genes of interest relative to Arbp using the following formula: $2^{-\Delta Ct\ (Gene-Arbp)}$.

Western blot analyses

Standard SDS-PAGE was performed. Each lane contained extracted protein from one FACS experiment. A total of three separate cell sorts were included in the analysis. We probed for GFP, GFAP, μ-crystallin and β-actin using rabbit anti-GFP (Invitrogen A11122), mouse anti-GFAP (Abcam ab4674), mouse anti- μ-Crystallin (Santa Cruz sc-376687) and rabbit anti-β-actin (Abcam ab8227) primary antibodies at 1:1000 dilution. The secondary antibodies IRDye 680RD anti-mouse (Li-Cor 926-68170) and IRDye 800CW anti-rabbit (Li-Cor 827-08365) were added to visualize the proteins using a Li-Cor Odyssey imager. Signal intensities were quantified with Image Studio Lite software (Li-Cor), and GFP, GFAP or μ-crystallin signals were normalized to β-actin.

QUANTIFICATION AND STATISTICAL ANALYSIS

Statistical tests were run in OriginPro 8.5/9/2015 or GraphPad Instat 3. Summary data are presented as mean ± s.e.m, with medians shown as a horizontal line where appropriate. Note that in some of the graphs, the bars representing the s.e.m. are smaller than the symbols used to represent the mean. For each set of data to be compared, we determined within GraphPad Instat or OriginPro whether the data were normally distributed or not. If they were normally distributed, we used parametric tests. If the data were not normally distributed, we used non-parametric tests. Paired and unpaired Student's two-tailed t tests (as appropriate) and two-tailed Mann–Whitney tests were used for most statistical analyses with significance declared at $p < 0.05$, but stated in each case with a precise *P value*. When the *P value* was less than 0.0001, it is stated as such to save space on the figure panels and text. *N* is defined as the numbers of cells, processes or mice throughout on a case-by-case basis depending on the particular experiment; the unit of analysis is stated in each figure or figure legend. When a statistical test was employed that was not a Student's t test or a Mann-Whitney test, then it is stated as such in the text and figure. Throughout the manuscript, the results of statistical tests (*P value*s and *n* numbers) are reported in full on the figure panels to save space in the main body of the manuscript. However, where appropriate key statistics are also reported in the text.

DATA AND SOFTWARE AVAILABILITY

The accession number for the raw and normalized RNA-seq data reported in this paper is GEO: GSE94010 (https://www.ncbi.nlm.nih.gov/geo). The accession number for the proteomic data reported in this paper is PRIDE: PXD005852.

ADDITIONAL RESOURCES

The RNA-seq and proteomic data of adult striatal and hippocampal astrocytes from this paper have been made available as a searchable website at http://astrocyternaseq.org. The RNA-seq data of adult cortical astrocytes from (Srinivasan et al., 2016) have also been included in the website.